PNAS
www.pnas.org

Supporting Information for

The $^{142}Nd/^{144}Nd$ variations in mantle-derived rocks provide constraints on the stirring rate of the mantle from the Hadean to the present

Eugenia Hyung and Stein B. Jacobsen

Eugenia Hyung
Email: ehyung@caltech.edu

This PDF file includes:

Supplementary text
Figs. S1 to S18
Tables S1 to S8
References for SI reference citations

www.pnas.org/cgi/doi/10.1073/pnas.2006950117

Supporting Information Text

Additional information on modeling of the Nd isotope data is in **sections 1-4** below. Considerations on how assimilation of Archean crust can generate μ^{142}Nd-anomalies in young basalts are discussed in **section 5**. Data reduction, analytical methods and samples are documented in **sections 6 and 7**. Data tables, data comparisons and data references are given in **sections 8-11**.

1. Calculations for crustal growth and recycling

Here we explain in more detail the calculations used for the comparison of the results of Rosas & Korenaga (2018) (1) with those of Jacobsen (1988) (2) and Jacobsen & Harper (1996) (3).

The exact solutions to the isotope and trace element evolution of a radioactive decay system for the crust-mantle recycling problem discussed here was given in Jacobsen & Wasserburg (1980) (4). In this case the mass of the continental crust (reservoir 3 with mass M_3) has initially zero mass (at time t = 0) and at that time all the mass is in the mantle (reservoir 3 with mass M_3). Conservation of mass requires $M_2(0) = M_2(t) + M_3(t)$. Jacobsen & Wasserburg (1980) (4) treated the mass transport problem with the following simple equation for the rate of growth of the mass of the crust:

$$\frac{dM_3}{dt} = \dot{M}_{23} - \dot{M}_{32}$$

where $\dot{M}_{23}$ is the rate of mass transfer from the mantle to the crust and $\dot{M}_{32}$ is the rate of recycling of continental crustal material back into the mantle. The mathematical solution to this problem was parametrized with $\psi(t) = \dot{M}_{23}/M_2$, which is the fractional rate of mass removal from the depleted mantle, in which $\phi(t) = \dot{M}_{32}/M_3$ is the fractional rate of mass removal from the continental crust. The reciprocals of ψ and ϕ are the instantaneous residence times for the bulk mass of reservoirs 2 and 3, respectively. The Jacobsen & Wasserburg (1980) (4) solution to this problem was obtained by substituting the definitions for ϕ and ψ into the equation above. The mass of the crust as a function of time is thus given by

$$M_3(t) = M_2(0)\exp[-\Psi(t) - \Phi(t)]\int_0^t \psi(\xi)\exp[\Psi(\xi) + \Phi(\xi)]d\xi$$

where

$$\Psi(t) = \int_0^t \psi(\xi)d\xi$$

and

$$\Phi(t) = \int_0^t \phi(\xi)d\xi$$

are the integrals of the fractional crustal addition and recycling rates, respectively.

The bulk mass flux of mantle melts into the crust ($\dot{M}_{23}$) carries elements like Nd and Sm that are strongly enriched relative to the mantle source. This enrichment is given by D-values defined by the average concentration in melt divided by the contemporaneous average concentration in mantle. At once the values for D_{Nd} and D_{Sm} are chosen/determined in addition to the mass evolution, then all the isotope and concentration evolutions can be

calculated for any isotopic decay system using the analytical solution in (4). The blue curves in the main text **Fig. 6** and **Figs. S1-S3** were calculated with $D_{Nd} = 27.5$, $D_{Sm}(t_s) = 14.4$, and the mass evolutions of Jacobsen (1988) [given in his **Figs. 4** and **5**, and Table 4] (2), constrained by least squares inversion of isotopic and elemental data. These parameters where later used by Jacobsen & Harper (1996) (3) to calculate the μ^{142}Nd isotopic evolution of the depleted mantle (their Fig. 16) as shown in **Fig. 6** of the main text and **Figs. S2** and **S3** of this supplement.

Rosas & Korenaga (2018) (1) carried out Monte Carlo simulation of the Nd isotope evolution. They also, in their Fig. 3 gave a red evolution curve that matches the median trend in their Monte Carlo results. This curve is given with well-defined parameters and we use it for comparison with their results. Their crustal growth curve (their equation 1) is:

$$\frac{M_3(t)}{M_3(t_p)} = \frac{1 - \exp[-\kappa_g(t - t_s)]}{1 - \exp[-\kappa_g(t_p - t_s)]}$$

with $\kappa_g = 17$, t_p is the present and t_s the starting point of crustal growth. Their recycling rate functions is (their equation 2):

$$\dot{M}_{32}(t) = R_s + (R_p - R_s)\frac{1 - \exp[-\kappa_r(t - t_s)]}{1 - \exp[-\kappa_r(t_p - t_s)]}$$

where R_s and R_p are the values of $\dot{M}_{32}$ at t_s and t_p, respectively. Their recycling function is defined by using $R_s = 2.0\times10^{22}$ kgGyr^{-1}, $R_p = 0.5\times10^{22}$ kgGyr^{-1}, and $\kappa_r = 0.5$. To compare with the above all that is needed is to calculate crustal addition rate ($\dot{M}_{23}$) is to calculate the derivative of the mass growth curve of the crust:

$$\frac{dM_3(t)}{dt} = \frac{\kappa_g M_3(t_p)\exp[-\kappa_g(t - t_s)]}{1 - \exp[-\kappa_g(t_p - t_s)]}$$

Then $\dot{M}_{23}$is the sum of dM_3/dt and $\dot{M}_{32}$. Using their parameters: $t_s = 4.51$Ga, $D_{Nd}(t_s) = 35$, $D_{Nd}(t_p) = 45$, $D_{Sm}(t_s) = 20$, $D_{Sm}(t_s) = 25$, and $f_m = 0.35$ (depleted mantle mass fraction), we have reproduced their results of the red ε^{143}Nd and μ^{142}Nd curves shown in the second row of their Fig. 3 (see main text **Fig. 6** and this supplement **Figs. S1-S3**). We have also in the supplement figures shown results for crustal residence time, $f^{Sm/Nd}$ in both the mantle and the continental crust, Nd concentration in the continental crust, ε^{143}Nd and μ^{142}Nd in the continental crust.

Jacobsen & Harper (1996) (3) also discussed a model (their Fig. 17) where the Hadean proto-crust is made by a distinct process from that responsible for the continental crust that develops later. For the results to be more directly comparable to the Rosas & Korenaga (2018) (1) results we used the following of their parameters: $t_s = 4.51$Ga, $D_{Nd}(t_s) = 35$, $D_{Nd}(t_p) = 45$, $D_{Sm}(t_s) = 20$, $D_{Sm}(t_s) = 25$, and $f_m = 0.35$ (depleted mantle mass fraction). However, the Hadean proto-crust grows to half the mass of the present continental crust at a constant rate the during the first 40 Myr (4.51 to 4.47), then no growth, and then the continental crust grows at a constant rate of growth from 4.0 Ga to the present. The recycling rate is constant at $\dot{M}_{32} = 0.7\times10^{22}$ kgGyr^{-1} between 4.0 Ga and the present and $\dot{M}_{32} = 0$ between 4.51 Ga and 4.0 Ga. The resulting isotope, element and mass evolution curves are all shown in green in the diagrams.

Here $f^{Sm/Nd}$ is defined to be:

$$f_i^{Sm/Nd} = \frac{\left({}^{147}Sm/{}^{144}Nd\right)_i}{\left({}^{147}Sm/{}^{144}Nd\right)_{CHUR}} - 1$$

and

$$\varepsilon_{143Nd} = \left[\frac{\left({}^{143}Nd/{}^{144}Nd\right)_i}{\left({}^{143}Nd/{}^{144}Nd\right)_{CHUR}} - 1\right] \times 10{,}000$$

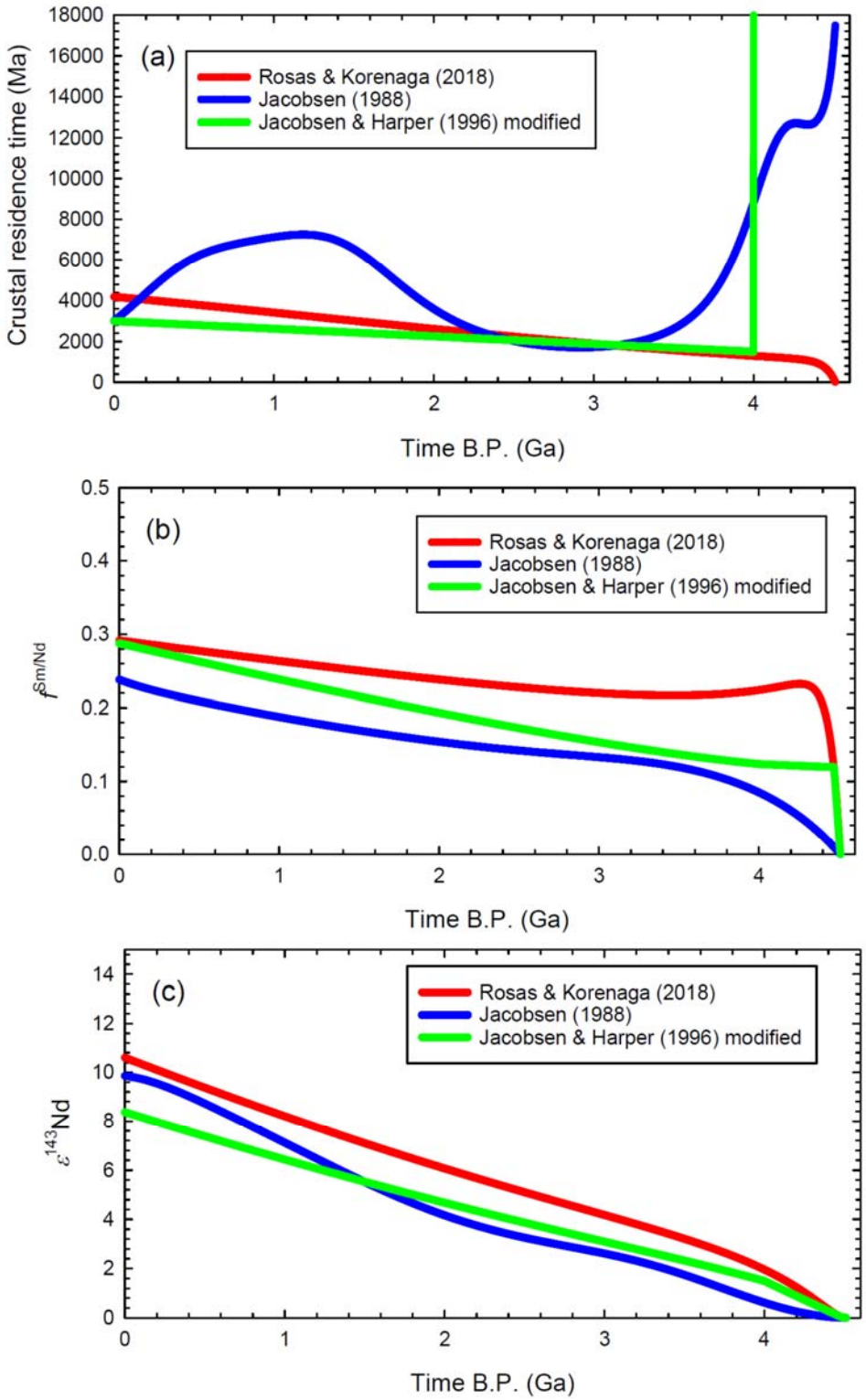

Fig. S1. The crustal residence time (a), the $f^{Sm/Nd}$ evolution of the depleted mantle (b), and the ε^{143}Nd-evolution of the depleted mantle (c).

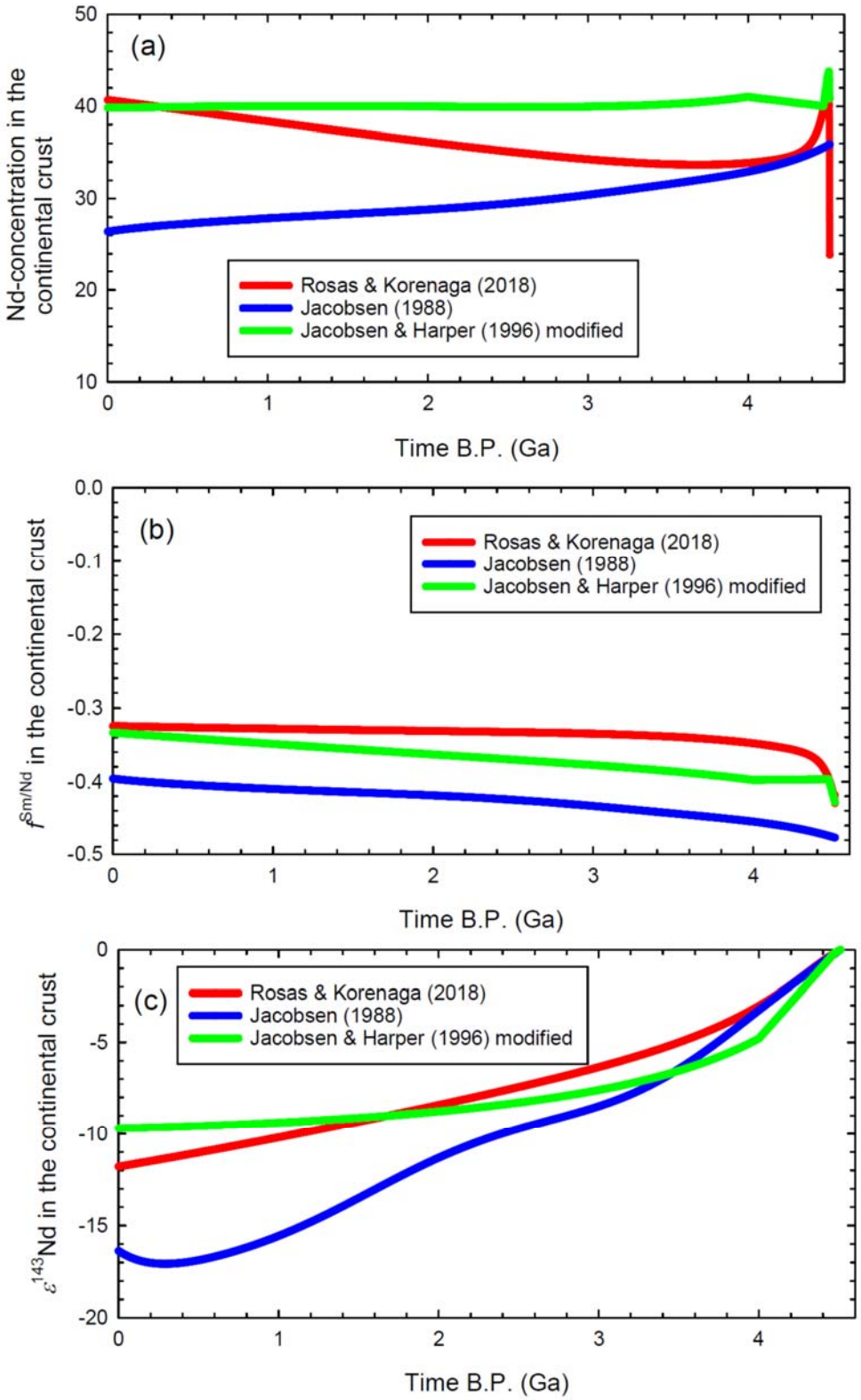

Fig. S2. The Nd concentration in the continental crust (a), the $f^{Sm/Nd}$ evolution of the continental crust (b), and the ε^{143}Nd-evolution of the continental crust (c).

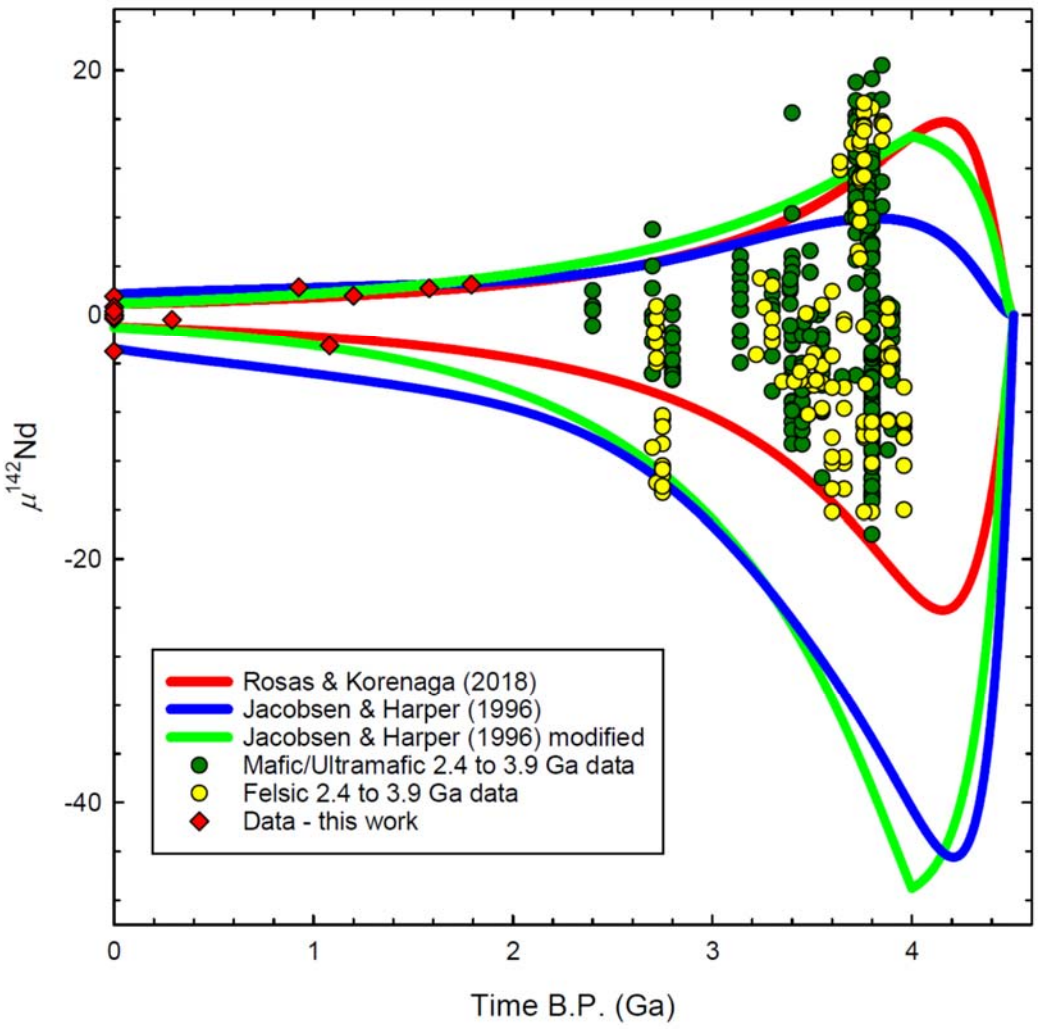

Fig. S3. The μ^{142}Nd-evolution of the continental crust and depleted mantle compared to the data of this work as well data of mafic/ultramafic and felsic rocks of 2.4 to 3.9 Ga age (Data source in Figure 3).

2. Model parameters for calculations for the stochastic mixing model for the mantle

The upper limit of the $^{143}Nd/^{144}Nd$ value of the early depleted reservoir can be constrained to a first degree based on observations of $^{143}Nd/^{144}Nd$ values of early terrestrial reservoirs. The $^{143}Nd/^{144}Nd$ value in turn is linked with the $^{147}Sm/^{144}Nd$ values of the early depleted reservoir by the relationship:

$$\frac{\varepsilon_{EDM}}{\varepsilon_{EEM}} = \frac{f_{EDM}}{f_{EEM}} = 1 - \frac{N_{BSE}(0)}{N_{EDM}(\tau)} = a \quad (4)$$

where $^{147}Sm/^{144}Nd_{CHUR}$ is 0.1967 (5), N_{EDM} is the total amount of a stable, nonradiogenic Nd species in the reservoir "EDM" at time τ, and a is a constant that determines the extent of depletion in the early depleted reservoir in relation to the Bulk Silicate Earth (BSE). N_{DM}/N_{BSE} for the modern-day depleted mantle is typically is observed

to be ~0.6. The extent to which the different layers are mixed are determined by the sizes of the reservoirs and their concentrations of Nd and are constrained by the above relation. The μ^{142}Nd value after the complete decay of ^{146}Sm (μ^{142}Nd is defined to be (^{142}Nd/^{144}Nd – ^{142}Nd/^{144}Nd$_{std}$)/^{142}Nd/^{144}Nd$_{std}$ x 1,000,000) is sensitive to the timing of differentiation and is dependent on the ^{147}Sm/^{144}Nd ratio of the early depleted reservoir through the relationship:

$$\left(\frac{^{142}Nd}{^{144}Nd}\right)_t^{EDM} = \left(\frac{^{142}Nd}{^{144}Nd}\right)_{t_p}^{BSE} + \frac{(^{146}Sm/^{144}Sm)_{t_0}}{(^{147}Sm/^{144}Sm)_{t_p}}\left[\left(\frac{^{147}Sm}{^{144}Nd}\right)_{t_p}^{BSE} e^{-\lambda_{146}t_d} + \left(\frac{^{147}Sm}{^{144}Nd}\right)_{t_p}^{EDM} (e^{-\lambda_{146}t} - e^{-\lambda_{146}t_d})\right]$$

where t_p is the time at present, t_0 is the time at the beginning of solar system history, and t_d is time passed from the time of differentiation. ^{146}Sm/^{144}Sm$_{t0}$ is set to be 0.00828 (6). The relationship between the mass of a reservoir (M), the concentration of Nd (C) in a reservoir, and the total amount of Nd (N) in each of the reservoirs are $M_{EDM}C_{EDM} = N_{EDM}$, Where the mass fraction of reservoir X_{EDM} is M_{EDM}/M_{BSE}, and $X_{EDM} + X_{EEM} = 1$.

Parameters that are capable of fitting extant μ^{142}Nd data were tested to be within a limited range. We use the values in the table below:

Table S1. Starting parameters that best accommodate Archean data distribution.

N_{EDM}/N_{BSE}	ε_{EDM}	ε_{EEM}	f_{EDM}	f_{EEM}	$\mu^{142}Nd_{EDM}$	$\mu^{142}Nd_{EEM}$
50%	26.6	-26.6	0.1782	-0.1782	20	-20

Here the timing of differentiation is set to be 100 Ma after solar system formation. The relative sizes of the early depleted and enriched reservoirs are also linked to the concentration of Nd in the reservoirs, for which we consider:

Table S2. Parameters that satisfy mass balance constraints.

l_{s3} (EDM)	l_{s2} (EEM)	M_{EDM}/M_{EEM}	C_{EDM}	C_{EEM}	Rate of mixing
2252	636	2.09	0.9232	1.935	500 Ma

where l_{s2} is the length scale of heterogeneity of reservoir "2," M_{EDM} is the mass of the early depleted mantle, and the average Nd concentration of the reservoirs are mass balanced so that the Bulk Silicate Earth concentration is 1.25 ppm (7).

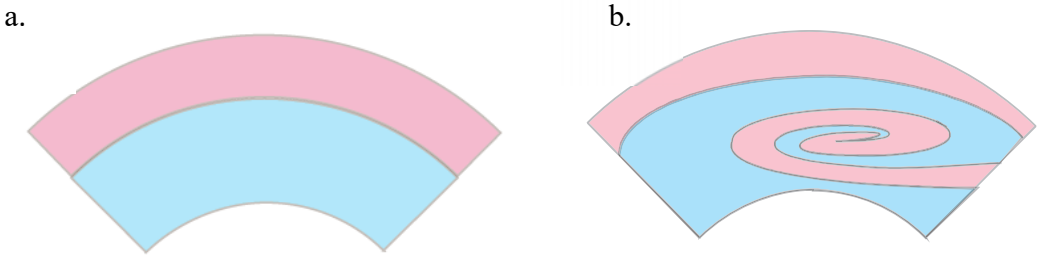

Fig. S4. a.) The two initial reservoirs are shown in different colors. b) The same two reservoirs after stretching and mixing.

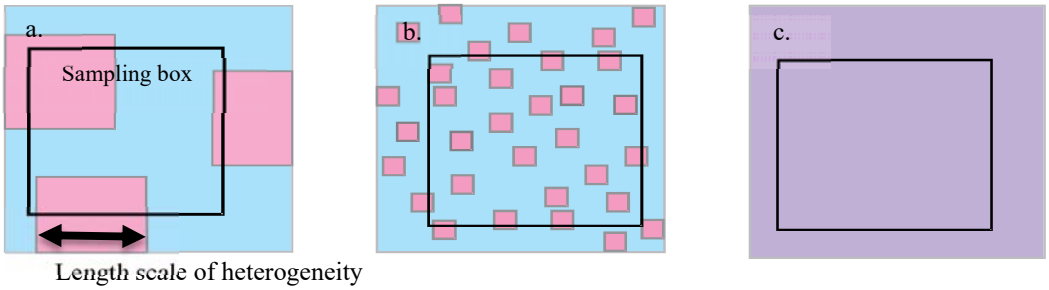

Fig. S5. a) The sampling box randomly placed in the mixture of different reservoirs at time T_a. b) At a later time T_b, the sizes of the different reservoirs have changed. c) Once the isotopic composition of the sampling box is indistinguishable from one another, the mantle is considered "homogeneous."

The timing at which the distribution of heterogeneity for the extinct $^{142}Nd/^{144}Nd$ variability starts to narrow, is determined by the relationship between the length scale of heterogeneity and the sampling box. In a simple experiment where the mantle differentiates into two homogeneous reservoirs, the sampled $^{142}Nd/^{144}Nd$ variability exhibits a bimodal distribution during when the length scale of heterogeneity is at least twice as long as the length scale of sampling. Isotopic variability in this scenario resemble a normal distribution near $\mu^{142}Nd = 0$ once the length scale of heterogeneity decreases beyond this threshold (8).

Plausible scenarios for the Earth's mantle to have started out with two reservoirs (one with depleted $^{142}Nd/^{144}Nd$ signature and one with enriched signature) are discussed in section 4.

3. Additional stirring and mixing model results to support our conclusions

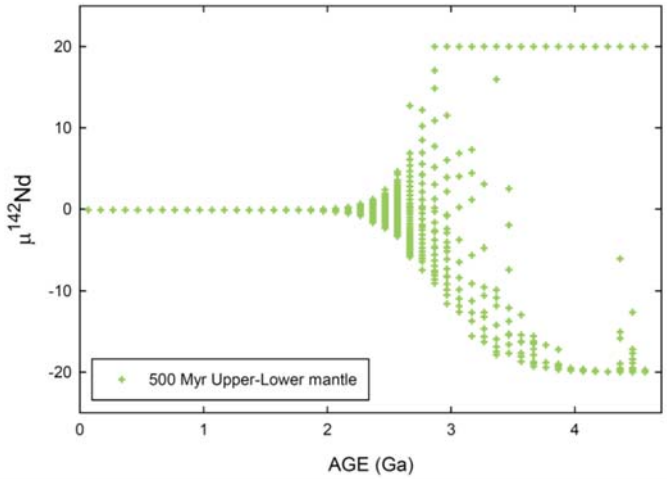

Fig. S6. Results for a stirring stirring rate of 500 Myr, spanning the volume of the upper mantle only, and an enriched reservoir whose thickness is 100 km. Due to the smaller mantle volume involved in mixing, the rate of homogenization of $^{142}Nd/^{144}Nd$ is faster, and the scenario cannot reproduce the $^{142}Nd/^{144}Nd$ data distribution at 2.7 Ga, whose $\mu^{142}Nd$ values range from +7 to –15 (9, 10).

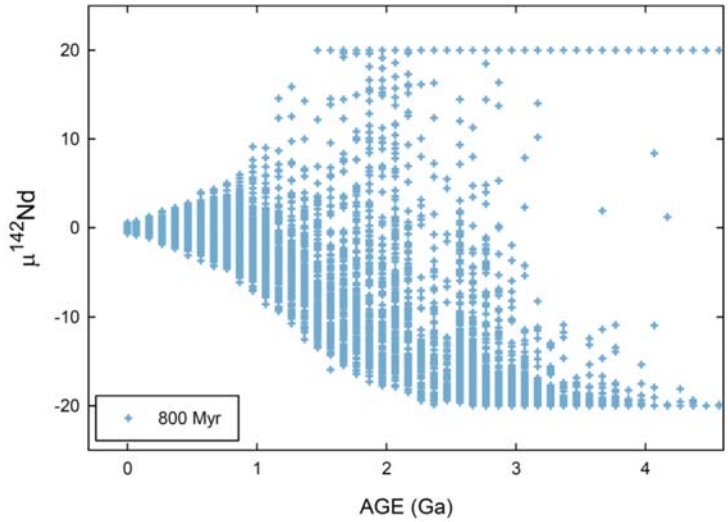

Fig. S7. Results for an 800 Myr stirring rate spanning the volume of the upper and lower mantle throughout the history of the Earth. Detectable μ^{142}Nd variations at the 2σ = ±5 ppm level are predicted to be widespread and common as recently as 1.0 Ga ago.

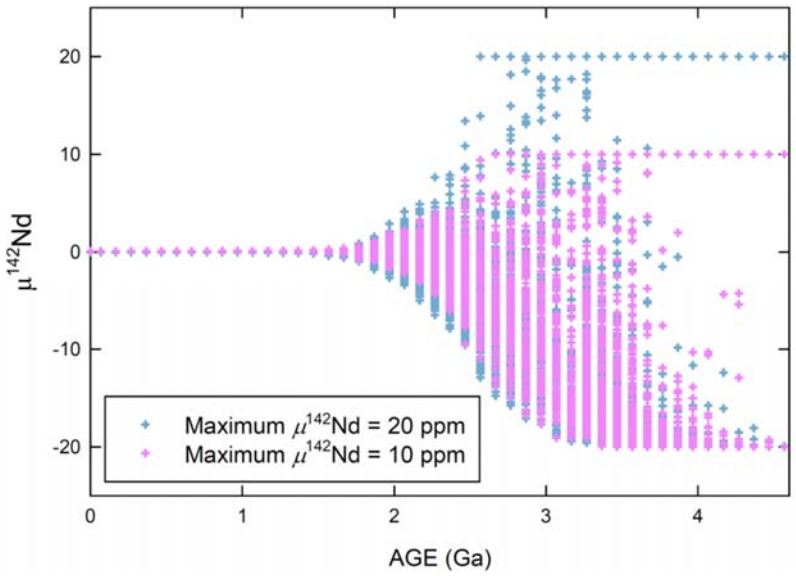

Fig. S8. The model parameters have here been adjusted according to mass balance so that the maximum μ^{142}Nd values of the early depleted reservoir are closer to 10 ppm (magenta). The model is run with a stirring rate of 500 Myr. These results are plotted on top of the model (blue) run with the same parameters (**Table SI 1,2**) presented in **Figure 3a**.

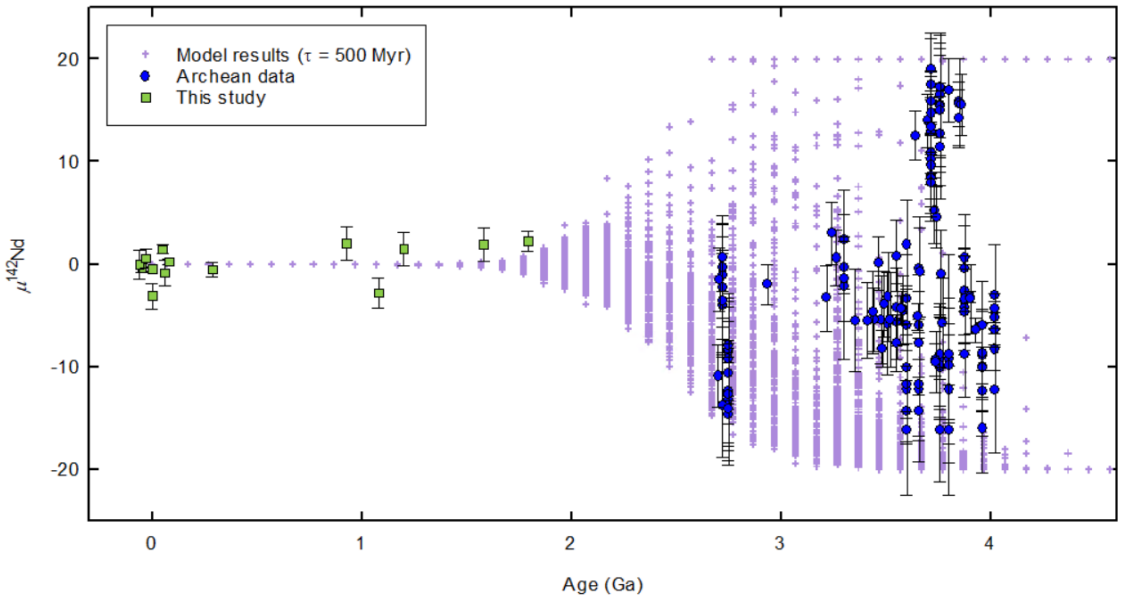

Fig. S9. Model results from a stirring rate of 500 Myr, considering μ^{142}Nd data from intermediate to felsic compositions for samples of 2.4 to 3.9 Ga age (data sources in Figure 3, with additional references from 11, 12).

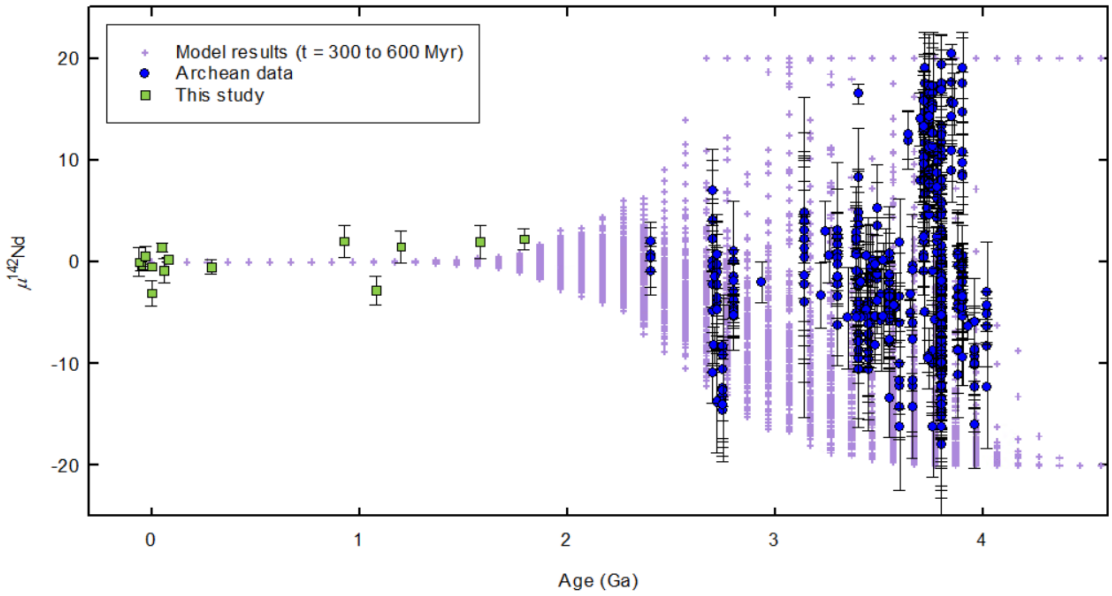

Fig. S10. Model results from the stochastic mixing model throughout time in comparison with μ^{142}Nd data throughout time, where a "fast" mantle stirring rate of 300 Myr is invoked during the Hadean up to 3.68 Ga, with a stirring rate of 600 Myr for the rest of Earth's history. A "dual" stirring rate provides a good fit to μ^{142}Nd data for a full range of compositions, ranging from ultramafic to felsic for samples of 2.4 to 3.9 Ga age (data source in Figure 3, with additional references from 11, 12).

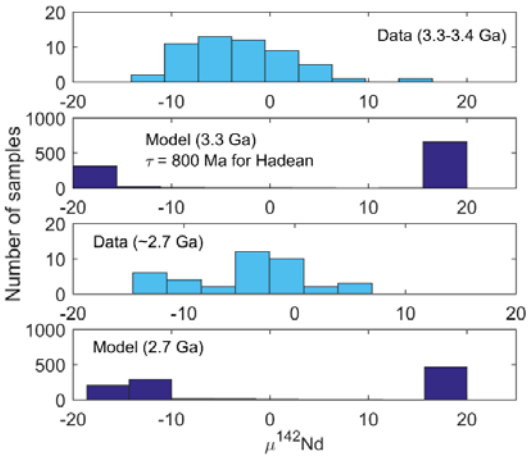

Fig. S11. Synthetic data distribution from the stochastic mixing model at 2.7 Ga, and 3.3 Ga, in comparison with data, where a "slow" mantle stirring rate of 800 Myr is invoked during the Hadean, with 500 Myr for the rest of Earth's history. In contrast to the data distribution at these time frames, at 3.3 Ga, depleted signatures are still expected to be dominant. At 2.7 Ga, enriched and depleted signatures are predicted to have an equal probability of being sampled.

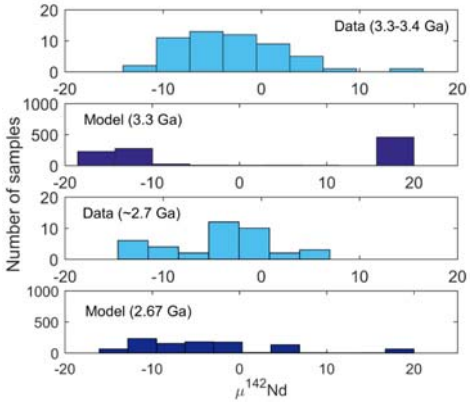

Fig. S12. Synthetic data distribution at 3.3 Ga, and 2.7 Ga (in comparison to data) where a relatively "fast" mantle stirring rate of 300 Myr is applied during the first ~800 Myr of Earth's history, with 600 Myr onwards. The synthetic data change over from having an abundance in depleted signatures to exhibiting more enriched signatures, better resembling the sampled data distribution.

4. The creation of initial μ^{142}Nd heterogeneities in the Early Earth

Initially the positive ε^{143}Nd and the positive μ^{142}Nd in the early mantle (3, 13, 14) were discussed mostly in terms a continental crust mantle evolution and recycling model (2, 15, 16). However, noble gas evidence pointed to an early magma ocean also being very important for the early differentiation of the Earth (16). As it became clear later that the early (Hadean and earliest Archean) mantle exhibit dominantly negative ε_{Hf} in contrast to the dominantly positive ε^{143}Nd values for early mantle this is evidence that an early magma ocean generated the dominant Nd and Hf isotopic heterogeneity in the early Earth (17, 18), rather than crust extraction and recycling. This inverse correlation between ε_{Hf} and ε^{143}Nd

is what is expected from fractionation in a deep magma ocean (primarily because of difference in melting-partitioning behavior with the involvement of lower-mantle minerals (19)). The later part of Earth history exhibits a positive correlation between ε_{Hf} and $\varepsilon^{143}Nd$ ($\varepsilon_{Hf} = \varepsilon^{143}Nd + 2$) as is expected for a scenario when the Lu-Hf and Sm-Nd fractionation during crustal extraction and recycling is dominated by melting in the upper mantle (20). Lu-Hf model ages based on Hf isotopes in zircons have so far not considered this difference between the early Nd and Hf isotope evolution of the mantle (21). Rosas and Korenaga (2018) (1) recently used the Nd isotope record (including ^{142}Nd) to argue for a constant continental crustal volume essentially since the origin of the Earth similar to the model favored by Armstrong (22). The Rosas and Korenaga (2018) (1) model is similar to the model of Jacobsen (1988) (2). However, Jacobsen (1988) (2) arrived at a continental crustal volume of 40% of the current volume at 3.8 Ga ago. The problem with any such model is how objectively one can establish the average Nd isotopic evolution of the mantle reservoir, because of the heterogeneous isotopic evolution of the mantle. The range of isotopic heterogeneity is much better established than the average curves through time and therefore Kellogg et al. (2002; 2007) (23, 24) developed a model to take this into account and used it for understanding the Nd, Sr and Pb isotopic heterogeneity in the Earth's mantle. The Kellogg et al. (2002; 2007) (23, 24) treatment was used for the long-lived isotopic systems in crust extraction and recycling model. Later this type of model was extended to extinct isotope systems such as ^{182}Hf-^{182}W and ^{146}Sm-^{142}Nd (8). The Jacobsen and Yu (2015) model (8) can equally well be applied to both a magma ocean scenario as well as for crust-mantle recycling. What is required are very early Earth processes that substantially fractionate Sm and Nd to produce both enriched and depleted early mantle reservoirs with a range of $\mu^{142}Nd$ from at least -20 to +20 ppm.

5. Generating modern-day $^{142}Nd/^{144}Nd$ heterogeneity through hypothetical crustal assimilation

Through simple mixing calculations, we find that it is possible to shift mantle values from $\mu^{142}Nd = 0$ to values of ±6 to ±7.4, with a crust whose $\mu^{142}Nd$ is ±20 (±2 ppm) using the parameters indicated in **Table S3**, with up to 5% of crustal assimilation through simple mixing as reflected in the Ce/Pb and Nb/U ratios (**Fig. S9** below). Similar Ce/Pb and Nb/U ratios are reflected particularly Piton des Neiges basalts in Reunion based on Ce/Pb and Nb/U ratios (green circles). The basalts from this flow also are reported in (25) to hold the widest range of variability in $\mu^{142}Nd$. In comparison, we note that calculations for the crustal material assimilation (26) into Mauritius lavas been estimated to be up to 3.5%, whose data is mostly based on zircons.

Such a hypothetical Archean crustal component would have to have a mildly positive $\varepsilon^{143}Nd$ composition, similar to the granitoids of Seychelles, to fit within the range of the variability in $\varepsilon^{143}Nd$ for Reunion lavas. The Nd concentration would be relatively high for this type of crust, up to 130-145 ppm, similar to K1714 (trachyandesite) or the Herefoss (HE-5) granite of our own study. Parameters used for $\varepsilon^{143}Nd$ calculations, are noted in the table below.

Table S3. Parameters used in calculations

	ε^{143}Nd	Nd concentration (ppm)
MORB	4.8 (chosen)	14.0 (ref. 27)
Hypothetical crust	1.7	135
Calculation Result	3.8	20.5
Reunion Lavas	3.8-4.8 (25)	13-33 (ref. 28)

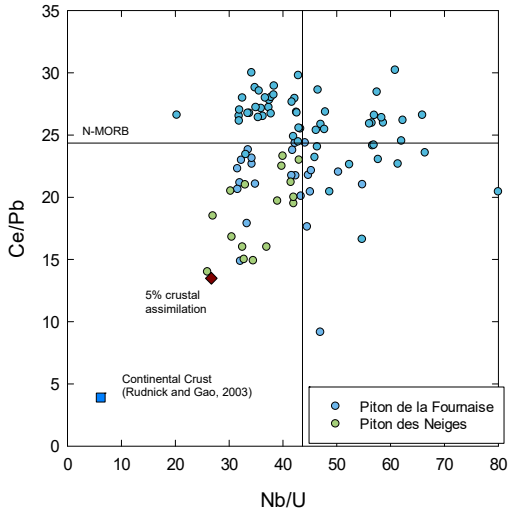

Fig. S13. The plotted circles are Ce/Pb vs Nb/U from Reunion basalts, and the red diamond represents 5% crustal assimilation into the average N-MORB composition (cross hairs), while the blue square represents Rudnick and Gao's (29) Ce/Pb and Nb/U ratios for the crust. The green dots represent the Piton des Neiges basalts, which also exhibit the most ^{142}Nd/^{144}Nd variability in (25). Average N-MORB Ce/Pb and Nb/U ratios are sourced from (27). Ce/Pb and Nb/U data for the Reunion basalts are from (28, 30, 31)

6. Data Reduction Methods and Analytic Technique

We describe two procedures for data reduction involving the exponential law (32) using a multi-dynamic method for the measurements of ^{142}Nd/^{144}Nd. The same two data collection sequences (labeled S1 and S2) are used in both procedures (**Table S4**). The methods were optimized for ^{142}Nd/^{144}Nd measurements. For a multi-dynamic procedure whose sequences are offset by only one mass unit, the ^{142}Nd/^{144}Nd measurement would depend on multiple isotope ratios. We therefore have chosen S1 and S2 to be offset by two mass units as shown in **Table S4** so ^{142}Nd/^{144}Nd is only dependent on the measurement of one additional isotope ratio (^{146}Nd/^{144}Nd). This way the measurements only depended on using the axial (Ax) and high2 (H2) Faraday cups. Small interferences of Ce and Sm were monitored in the L2 and H5 cups.

Table S4. Sequence set-up for multi-dynamic method.

	L2	Ax	H2	H5
Sequence 1(t_1)	^{140}Ce	^{142}Nd	^{144}Nd	^{147}Sm
Sequence 2(t_2)		^{144}Nd	^{146}Nd	

We did not measure the other Nd isotopes (^{143}Nd, ^{145}Nd, ^{148}Nd and ^{150}Nd) as part of this procedure because it would result in poorer quality ^{142}Nd/^{144}Nd measurements. The ^{143}Nd/^{144}Nd measurements reported in **Table S6** were determined in separate shorter static and/or multi-dynamic measurements.

We derived two reduction methods from this set-up. The two multi-dynamic data reduction methods here called "Reduction 1: RED1" and "Reduction 2: RED2". As discussed below, a standard multi-dynamic ^{142}Nd/^{144}Nd measurement (RED1) has a residual term that cannot be canceled out or evaluated, while our new method (RED2) doesn't. Therefore, the RED2 method was used to cancel out effects of different efficiencies (*f*) for individual Faraday cups.

The data was all acquired with the Nd-142 intensity kept ideally within a ±1% window of 7 volts (10^{11} ohm resistors). Then to obtain precise ratios, all ion beam intensities were corrected for time-dependent drift by the following method.

Drift corrections: For both methods, the data are corrected for drift by using time interpolation to correct for either intensity changes or isotope ratio changes. The basis for drift correction is the observed changes in intensity or ratios between two sequences, that would have otherwise assumed to have been measured concurrently.

Time interpolation drift correction is based on repeated measurements of ^{146}Nd (which has no interferences) to correct the t_2-values back to t_1. The ^{146}Nd intensities measured in H2 were used to correct ^{144}Nd from S2 to t_1 and ^{146}Nd from S2 also to t_1. This was done using least-squares fitting of the ^{146}Nd signal in H2 with a fourth order polynomial over 1 block (20 cycles; 10 cycles each from Sequence 1 and Sequence 2) as a function of time. We use Matlab to code this function. The main Matlab function used for drift corrections is `polyfit(x,y,a)`. It fits "y" into a polynomial of degree "a" as a function of "x". Example:

```
parameter1=polyfit(timestring,intensity146,4)
```

Here "timestring" is the string which contains the time at which the corresponding ^{146}Nd intensity is recorded, while "intensity146" is a string that contains intensities of ^{146}Nd. Normalization would take the form of:

```
polynomial146 = timestring^4*parameter1(1)+
timestring^3*parameter1(2)+ timestring^2*parameter1(3)+
timestring*parameter1(4)+parameter1(5)
Normalized_intensity=intensity146./polynomial146.*intensity
146(c)
```

Here "polynomial146" is the name of a newly created string, while "c" is the first intensity of the corresponding block. Although it is possible to normalize the cycles from

Seq2 just to the sequence directly preceding it, we chose to normalize the cycles to the first intensity of the block, to prevent overcorrection due to noise while accommodating for the total change in signal intensity within the block. The isotope ratios at t_1 were then calculated by using the polynomial for ^{146}Nd to calculate both $^{146}Nd^{S2}(t_1)$ and $^{144}Nd^{S2}(t_1)$, assuming they both have the same time variability. After these drift corrections, we obtained:

$$\left(\frac{^{142}Nd^{(S1)}(t_1)}{^{144}Nd^{(S2)}(t_1)}\right)_M = \frac{I^{(S1)}_{142}(t_1)}{I^{(S2)}_{144}(t_1)} \times \frac{f_{Ax}}{f_{Ax}} = \frac{I^{(S1)}_{142}(t_1)}{I^{(S2)}_{144}(t_1)} \qquad (10)$$

$$\left(\frac{^{146}Nd^{(S2)}(t_1)}{^{144}Nd^{(S1)}(t_1)}\right)_M = \frac{I^{(S2)}_{146}(t_1)}{I^{(S1)}_{144}(t_1)} \times \frac{f_{H2}}{f_{H2}} = \frac{I^{(S2)}_{146}(t_1)}{I^{(S1)}_{144}(t_1)} \qquad (11)$$

Assuming that the data follow the exponential law, the RED2 method gives:

$$\left(\frac{^{142}Nd}{^{144}Nd}\right)^{\exp(RED2)}_N = \frac{I^{(S1)}_{142}(t_1)}{I^{(S2)}_{144}(t_1)} \left[\frac{\frac{I^{(S2)}_{146}(t_1)}{I^{(S1)}_{144}(t_1)}}{0.7219}\right]^{-p} \qquad (12)$$

Note that the cup factors again cancel out completely in this derivation. Comparison of **Figs. 1a** and **1b** shows that RED2 yield far superior reproducibility compared to RED1. The RED2 method results in an external reproducibility of = ±1.7 ppm (2σ) (**Fig. S12** and **Table S6**).

The matlab code to implement the drift corrections is as follows:

```
function
intdrift_corr(N,filename_in,sheet,filename_out,output)
%N=number of cycles in block
%filename_in= excel input file name ('input.xlsx')
%sheet= sheet name (e.g., 'Sheet1')
%filename_out=output file name (e.g., 'output.xlsx')
%output= sheet name in output file ('drift_corr')
%Example command line:
%intdrif_corr(20,'input.xlsx','Sheet1','output.xlsx','Sheet
1')
%read in data
timestring=xlsread(filename_in,sheet,'B2:B3000');
%time, usually in seconds
S1_S2_142=xlsread(filename_in,sheet,'D2:D3000');
S1_S2_144=xlsread(filename_in,sheet,'F2:F3000');
S1_S2_146=xlsread(filename_in,sheet,'G2:G3000');
%corresponding intensities (beams for mass 142, 144, 146,
respectively; signal intensities from S1 and S2 are
staggered)
first_int=xlsread(filename_in,sheet,'H2:H3000');
%first intensities of each block for 146Nd, organized in
column "H"
count20=round(nnz(S1_S2_142)./N);
 for i=0:count20-1
```

```
for c=1+i*N:i*N+N
p(c,:)=polyfit(timestring((1+i*N):(i*N+N)),S1_S2_146((1+i*N
):(i*N+N)),4);
    % "4" indicates 4th degree polynomial
end
%polynomial fitting to data, 4th degree
 end
p_flip=fliplr(p);
% countp=size(p);
% countp=countp(1,2);
countp=5;
 %4th degree polynomial
    for i=0:count20-1;
        for c=1+i*N:i*N+N;
            for pc=1:countp %for terms up to the "countp-
1"th degree as indicated by "countp"
polynom_save(c,pc)=p_flip(c,pc).*timestring(c).^(pc-1);
            end
        end
     end
 %calculate polynomial
    for i=0:count20-1;
        for c=1+i*N:i*N+N;
polynom_save1(c)=sum(polynom_save(c,:));
        end
    end
%calculate polynomial (cont.)
        for i=0:count20-1;
   for c=1+i*N:i*N+N;
S1_S2_142_intdrift_corr(c)=S1_S2_142(c)./polynom_save1(c).*
first_int(i+1);
S1_S2_144_intdrift_corr(c)=S1_S2_144(c)./polynom_save1(c).*
first_int(i+1);
S1_S2_146_intdrift_corr(c)=S1_S2_146(c)./polynom_save1(c).*
first_int(i+1);
% lines for intensity normalization
   end
        end
%commands for printing data in designated output excel
file:
xlswrite(filename_out,
S1_S2_142_intdrift_corr,output,'B2:B3000')
%adjust "B3000" to appropriate number of data points
xlswrite(filename_out,
S1_S2_144_intdrift_corr,output,'C2:C3000')
xlswrite(filename_out,
S1_S2_146_intdrift_corr,output,'D2:D3000')
```

```
end
```

Then, the data were interference corrected and isotope ratios were calculated and stored in a data file. This data file was filtered for outliers through Chauvenet's criterion, as outlined below:

Filtering of data.

For rejection of data we use *Chauvenet's criterion.* It states that a measurement may be rejected if the probability of obtaining it is less than *1/2N*, where N is the total number of measurements. Thus, we want to find the value of T such that P(T) = 1 – 1/2N. Assuming normally distributed data, the probability for a measurement to occur in an interval within Tσ (σ = standard deviation) of the mean is:

$$P(T) = \frac{1}{\sqrt{2\pi}} \int_{-T}^{T} e^{-\frac{x^2}{2}} dx = \text{erf}(\frac{T}{\sqrt{2}})$$

This means that for 10 measurements we want to find the value of T such that P(T) = 1 – 1/20 = 0.95 and this gives T = 1.96. This means that an observation that is more than 1.96σ away from the mean can be rejected. For N = 20 the limit is 2.24. For N = 50 the limit is 2.57σ. Typically, we analyze the data in blocks of 20 measurements at a time to filter out outliers. The matlab code to implement this procedure is as follows:

```
function filtering(N,filename_in,sheet,filename_out,output)
%% N = number of measurements from block to filter
%% filename_in = name of input excel file, where data are
arranged and normalized for drift corrections
% and corrected for interference
%% sheet = name of input sheet
%% filename_out = name of output excel file
%% output = name of output sheet
% example:
filtering(20,"Input.xlsx','Sheet1','Output.xlsx','Sheet1')
S1_S2_142=xlsread(filename_in,sheet,'B2:B3000');
%hopefully your data is arranged in columns, otherwise,
code must be
%modified accordingly
S1_S2_144=xlsread(filename_in,sheet,'C2:C3000');
S1_S2_146=xlsread(filename_in,sheet,'D2:D3000');
% read in data here
P=1-1/(2*N);
T=erfinv(P);
%inverse error function
T=T*sqrt(2);
count20=round(nnz(S1_S2_142)./N);
%round number of blocks
total=size(S1_S2_142);
total=total(1);
%total number of data points from string
```

```
c=0;
% reset counts
average1=mean(S1_S2_146);
stdev1=std(S1_S2_146);
count=0;
filter_count=0;
%reset counts
average_sum=0;
c=0;
 for i=0:count20-1
for c=1+i*N:i*N+N
      %filtering
if S1_S2_146(c) < average1+T*stdev1 && S1_S2_146(c) >
average1-1.T*stdev1;
      S1_S2_144_2(c)=S1_S2_144(c);
     S1_S2_142_2(c)=S1_S2_142(c);
     S1_S2_146_2(c)=S1_S2_146(c);
      %record values in new separate string "S1_S2_144_2"
      average_sum=average_sum+S1_S2_146(c);
      count=count+1;
      filtered(c)=0;
else
    % don't include filtered values in new separate results
string "S1_S2_146_2"
      count=count + 0;
      filter_count=filter_count+1;
      filtered_144(c)= S1_S2_144(c);
     filtered_142(c)= S1_S2_142(c);
     filtered_146(c)= S1_S2_146(c);
    % put filtered numbers in alternative string "filtered"
end
end
tot_count=filter_count+count;
count;
average(i+1)=sum(S1_S2_146)/tot_count
% average before filtering
ste_notfiltered(i+1)=std(S1_S2_146)/sqrt(tot_count)
% standard error before filtering
average_filtered(i+1)=average_sum/count
% average after filtering
to_std=0;
count20=round(nnz(S1_S2_144)./N);
%script for standard error after filtering
    c=0;
for c=1+i*10:i*10+N
    if S1_S2_146 (c) < average1+T*stdev1 && S1_S2_146 (c) >
average1-1.T*stdev1;
```

```
      to_std=to_std+(S1_S2_146_2(c)-average_filtered).^2;
% variance
    else
      to_std=to_std+0;
    end
end
std_filtered(i+1)=sqrt(to_std(i+1)./N)
%st dev after filtering
ste_filtered(i+1)=std_filtered(i+1)./sqrt(N)
%st err after filtering
end
results2(results2==0) = NaN;
filtered(filtered==0) = NaN;
% Print strings in new excel file
xlswrite(filename_out, S1_S2_142_2',output,'C2:C3000')
xlswrite(filename_out, S1_S2_144_2',output,'D2:D3000')
xlswrite(filename_out, S1_S2_146_2',output,'E2:E3000')
xlswrite(filename_out,filtered_142',output,'F2:F3000')
xlswrite(filename_out,filtered_144',output,'F2:F3000')
xlswrite(filename_out,filtered_146',output,'F2:F3000')
end
```

Then the data was reduced by the following two (old & new) multi-dynamic methods. The filtering produced very little improvement, affecting the 2σ external reproducibility at the 2nd digit.

Multi-dynamic Reduction 1 (RED1): In this method, the $^{142}Nd/^{144}Nd$ ratio obtained in the first sequence (S1) at time t_1 is based on the measurement of ion beam intensities (I) of ^{142}Nd ($I_{142}^{S1}(t_1)$) and ^{144}Nd ($I_{144}^{S1}(t_1)$) in the axial (Ax) and H2 cups. The second sequence is the measurement of ^{144}Nd ($I_{144}^{S2}(t_2)$) and ^{146}Nd ($I_{146}^{S2}(t_2)$) in the Ax and H2 cups at time t_2. The selected isotope ratios used in RED1 are outlined in bold in the table below:

	L2	Ax	H2	H5
Sequence 1(t_1)	^{140}Ce	**^{142}Nd**	**^{144}Nd**	^{147}Sm
Sequence 2(t_2)		**^{144}Nd**	**^{146}Nd**	

These isotope ratios, measured in S1 and S2, depend on the measured ion beam intensities (I), and also the unknown Faraday cup factor efficiencies for the axial (f_{Ax}) and high2 (f_{H2}) Faraday cups as follows:

$$\left(\frac{^{142}Nd}{^{144}Nd}\right)_M^{(S1)} = \frac{I_{142}^{(S1)}(t_1)}{I_{144}^{(S1)}(t_1)} \times \frac{f_{Ax}}{f_{H2}} \qquad (1)$$

$$\left(\frac{^{146}Nd}{^{144}Nd}\right)_M^{(S2)} = \frac{I_{146}^{(S2)}(t_2)}{I_{144}^{(S2)}(t_2)} \times \frac{f_{H2}}{f_{Ax}} \qquad (2)$$

The subscript M refers to raw measured ratios, not corrected for mass spectrometric fractionation. In this method, time dependent drift is corrected with respect one of the isotope ratios. This is because we measure the $^{142}Nd/^{144}Nd$ and $^{146}Nd/^{144}Nd$ ratios at different times, and $^{146}Nd/^{144}Nd$ is used for mass fractionation correction of $^{142}Nd/^{144}Nd$. Thus, linear interpolation of $^{146}Nd/^{144}Nd$ ratios is used to obtain the ratio of $^{146}Nd/^{144}Nd$ corresponding to the time when $^{142}Nd/^{144}Nd$ is measured (t_1).

$$\left(\frac{^{146}Nd}{^{144}Nd}\right)_M^{(S2)} = \frac{I_{146}^{(S2)}(t_1)}{I_{144}^{(S2)}(t_1)} \times \frac{f_{H2}}{f_{Ax}} \qquad (3)$$

We have found that this accounts for up to a 2 ppm correction using this dynamic sequence. The exponential law (1) for $^{142}Nd/^{144}Nd$ corrected for mass spectrometric mass dependent fractionation using $^{146}Nd/^{144}Nd$ is:

$$\left(\frac{^{142}Nd}{^{144}Nd}\right)_N^{\exp} = \left(\frac{^{142}Nd}{^{144}Nd}\right)_M \left[\frac{\left(\frac{^{146}Nd}{^{144}Nd}\right)_M}{0.7219}\right]^{-p} \qquad (4)$$

The subscript N refers to measured ratios, corrected for mass spectrometric fractionation and the superscript *exp* refers to the exponential law being used for the fractionation correction using $^{146}Nd/^{144}Nd = 0.7219$ for the normalization value. The exponent, p in the exponential law is given by:

$$p = \frac{\ln(m_{142Nd}/m_{144Nd})}{\ln(m_{146Nd}/m_{144Nd})} = \frac{\ln(141.907729/143.910093)}{\ln(145.913123/143.910093)} = -1.0137$$

where the m's represent the masses of the individual isotopes.

If we assume that the data obey the exponential law, then there is no complete cancellation of cup factors in the RED1 method:

$$\left(\frac{^{142}Nd}{^{144}Nd}\right)_N^{\exp(RED1)} = \frac{I_{142}^{(S1)}(t_1)}{I_{144}^{(S1)}(t_1)} \times \frac{f_{Ax}}{f_{H2}} \left[\frac{\frac{I_{146}^{(S2)}(t_1)}{I_{144}^{(S2)}(t_1)} \times \frac{f_{H2}}{f_{Ax}}}{0.7219}\right]^{-p} \qquad (5)$$

The cup factors can be factored out separately:

$$\left(\frac{^{142}Nd}{^{144}Nd}\right)_N^{\exp(RED1)} = \frac{I_{142}^{(S1)}(t_1)}{I_{144}^{(S1)}(t_1)} \left[\frac{\frac{I_{146}^{(S2)}(t_1)}{I_{144}^{(S2)}(t_1)}}{0.7219}\right]^{-p} \left(\frac{f_{H2}}{f_{Ax}}\right)^{-1-p} \qquad (6)$$

where

$$\left(\frac{f_{H2}}{f_{Ax}}\right)^{-1-p} \qquad (7)$$

is the unknown cup factor ratio. While the power law ($p = -1$ in Eq. 4) is capable of cancelling out this residual term in the multi-dynamic reduction, the exponential law doesn't, resulting in this small residual.

Multi-dynamic Reduction 2 (RED2): In contrast to RED1, this reduction method is capable of cancelling out residual terms. The data collection sequence (S1) measures ^{142}Nd and ^{144}Nd in the Ax and H2 cups. The isotopic ratio is calculated from the ion beam intensities (I) and the cup efficiency factors (f). The second data collection sequence (S2) measures ^{144}Nd and ^{146}Nd in the Ax and H2 cups. The selected isotope ratios for this method are outlined in bold in the table below:

	L2	Ax		H2	H5
Sequence 1(t_1)	^{140}Ce	**^{142}Nd**		**^{144}Nd**	^{147}Sm
Sequence 2(t_2)		**^{144}Nd**		**^{146}Nd**	

These isotope ratios depend on the measured ion beam intensities (I), but not on the unknown Faraday cup factor efficiencies (f). The latter cancel out as shown below:

$$\left(\frac{^{142}Nd^{(S1)}(t_1)}{^{144}Nd^{(S2)}(t_2)}\right)_M = \frac{I_{142}^{(S1)}(t_1)}{I_{144}^{(S2)}(t_2)} \times \frac{f_{Ax}}{f_{Ax}} = \frac{I_{142}^{(S1)}(t_1)}{I_{144}^{(S2)}(t_2)} \qquad (8)$$

$$\left(\frac{^{146}Nd^{(S2)}(t_2)}{^{144}Nd^{(S1)}(t_1)}\right)_M = \frac{I_{146}^{(S2)}(t_2)}{I_{144}^{(S1)}(t_1)} \times \frac{f_{H2}}{f_{H2}} = \frac{I_{146}^{(S2)}(t_2)}{I_{144}^{(S1)}(t_1)} \qquad (9)$$

The two data reduction methods (RED1 and RED2) differ by the unknown cup factor ratio (Eq. 5), which can be calibrated by comparing the ratios of the intensities of ^{144}Nd(S1) and ^{144}Nd(S2).

Comparison of **Figs. 1a** and **1b** shows that RED2 yield far superior reproducibility compared to RED1. The RED2 method results in an external reproducibility of = ±1.7 ppm (2σ) (**Fig. S12** and **Table S6**).

The two data reduction methods (RED1 and RED2) differ by the unknown cup factor ratio (Eq. 5), which can be calibrated by comparing the ratios of the intensities of ^{144}Nd(S1) and ^{144}Nd(S2).

Combining equations (6) and (12) we obtain:

$$\frac{\left(\frac{^{142}Nd}{^{144}Nd}\right)_N^{\exp(RED1)}}{\left(\frac{^{142}Nd}{^{144}Nd}\right)_N^{\exp(RED2)}} = \left(\frac{f_{H2}}{f_{Ax}}\right)^{-1-p} \qquad (13)$$

where

$$\frac{f_{H2}}{f_{Ax}} = \frac{I_{144}^{(S1)}(t_1)}{I_{144}^{(S2)}(t_1)} \qquad (14)$$

This equation can be reorganized to the following relationship that is the basis for **Fig. 1c**.:

$$\left[\left(\frac{f_{H2}}{f_{Ax}}\right)^{-1-p}-1\right]10^6=\left(\frac{^{144}Nd}{^{142}Nd}\right)_N^{\exp(RED2)}\left[\left(\frac{^{142}Nd}{^{144}Nd}\right)_N^{\exp(RED1)}-\left(\frac{^{142}Nd}{^{144}Nd}\right)_N^{\exp(RED2)}\right]10^6 \quad (15)$$

This equation quantifies the relationship between the two reduction methods, linking the discrepancy in $^{142}Nd/^{144}Nd$ values (RED1 – RED2) to variability of the cup factor ratio. The slope of the data in this diagram should be $^{144}Nd/^{142}Nd = 0.876$. The best fit to the standard data in **Fig. 1c** yields a slope of 0.75 ±0.06. If the samples are included, then the slope is 0.80 ±0.15, within error of the theoretical value. Samples that lie off the linear trend, can possibly be attributed to mixing of multiple reservoirs on the filament. Terrestrial sample measurements (orange) that are offset from the standard trend include one measurement of the following samples: DICE, HLY102-096, RAM-3, and E-58, and the two GN-12-03 measurements. JNdi-1 in RED1 is offset from RED2 by ~ -4 ppm on average.

$^{146}Nd/^{144}Nd$ ratios: We find that data that do not monotonically increase in $^{146}Nd/^{144}Nd$ may be reflections of reservoir mixing processes (e.g., signals that increases, then decreases, or vice-versa). We also find that $^{146}Nd/^{144}Nd$ may occasionally flatten instead of monotonically increasing after a certain point. Similarly to what is acknowledged and described in (33), we filter out the portion of the data at the end of a run where this occurs, before the bend, but do not reject the whole run.

Loading technique: Samples were loaded on a single side filament of a triple filament arrangement. 1 µL of sample was ideally loaded in 6 increments, and 2 µL we found would equal about 11-13 loads. All loads were strictly hand-controlled. After the sample was loaded and dried down at 0.6 A on the filament, we added 1 drop of 0.5 N phosphoric acid and dried down the filament at about 1.5 A for 2.5 minutes. Then the filament was flashed at a little over 2 A for 3 seconds. The filaments are degassed in a standard Isotopx filament degasser. After degassing, we waited for at least two days prior to loading the filament. The loading technique was important in consistency of runs and preventing reverse fractionation effects.

Measurements on the Thermal Ionization Mass Spectrometer: To make $^{142}Nd/^{144}Nd$ measurements, Nd aliquots that were purified through column chromatography (~1000-1500 ng) were loaded on 99.999% triple Re zone-refined filament (H Cross, USA) at ~0.6 A. The Nd isotope measurements were carried with an Isoprobe T (HCT010) thermal ionization mass spectrometer equipped with new Xact amplifiers with 10^{11} Ω resistors. A gains calibration was carried out prior to each measurement. The side filaments were ramped to an average of 2.3A and the center filament up to 4.5 A. The isotope data were collected at 5 (n=3), 6 (n=2) or 7 V (n=55) for with an integration time of 10 secs per cycle, with ramping of the sample filament in between blocks to match the starting intensity. Magnet settling time was 2 secs. Prior to each block consisting of 10 cycles for each sequence, half-mass baseline measurements were carried out for 10 secs with an automatic peak centering routine. The number of cycles for each sample ranged from 150 to 2000 cycles, with an average of 500. Typical ^{142}Ce interferences for ^{142}Nd were less than 1 ppm, as with ^{144}Sm interferences for ^{144}Nd.

$^{147}Sm/^{144}Nd$ ratios were determined from concentration measurements of small dissolved aliquots of whole rock samples measured for major and trace elements using the iCAP Q. Samples and standards were doped with 10 ppb In for drift corrections.

7. Sample characterization

Major and trace element data for the samples are given in **Table S5**. Rare earth element patterns for the MORBs and OIBs are shown in **Fig. S10**. KN207-2 (24.913 to 24.920ºN, 45.578 to 45.570ºW) is an Atlantic N-MORB. CH59-2 (8.000ºN, 102.840ºW) is also an N-MORB from the East Pacific Rise whose provenance is free from hotspot and subduction zone influences. A12DR44 (35.326ºN, 34.859ºE) is characterized as an EM1 MORB. HLY102-096 (86.14ºN, 31.78ºE) is a slightly enriched MORB from the Gakkel ridge free from hot spot influences (34). RC2D-1 is a HIMU MORB from the south Atlantic (35, 36). DICE is a depleted Icelandic plume sample that has been used for extensive noble gas isotope studies (37–39). BHVO-2 is an OIB from the Kilauea crater of Hawaii (40).

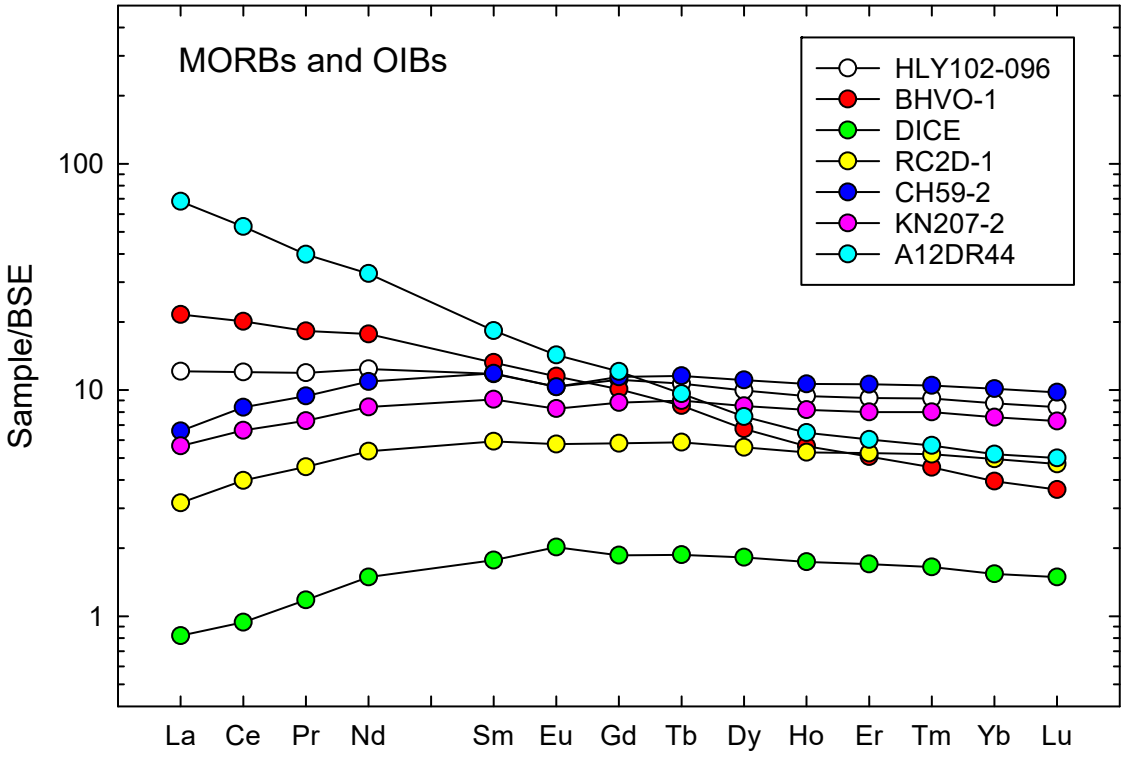

Fig. S14. Plot of rare earth elements (REEs) for young ($T = 0$) MORBs and OIBs.

Samples from the Baltic Shield area range in compositions from gabbroic to granitic. They are representative of the established $^{143}Nd/^{144}Nd$ evolution of the source of the Baltic Shield through this time period and also similar to the global evolution (41). Rare earth element patterns for the Baltic Shield samples are shown in **Fig. S11**. K410 is a sample of the Vinoren gabbro from the Kongsberg sector of S. Norway. It is characterized by a relatively flat MORB-like REE pattern and its age is 1.20 Ga (42). E-58 (from Oevre Eiker) a 1.58 Ga deep crustal granulite facies quartz diorite (42) from the Kongsberg sector of S. Norway. RAM-3 (from Raftsund) is a 1.792 Ga medium-coarse grained deep crustal mangerite rich in K-feldspar (43) from the Lofoten area of N. Norway. GN-12-03 (from Gardnos) is a 1.08 Ga upper crustal granite (44) from right north of the Gardnos impact crater in Hallingdal of S. Norway. HE-5 (from Herefoss) is a coarse-grained 0.926 Ga upper crustal granite (45) with a negative Eu anomaly and from the Bamble sector of S. Norway. K1714 is a trachy-andesite with an age of 288 Ma that is highly enriched in light rare earth elements (46) and from the Krokskogen area of the Oslo Rift of S. Norway.

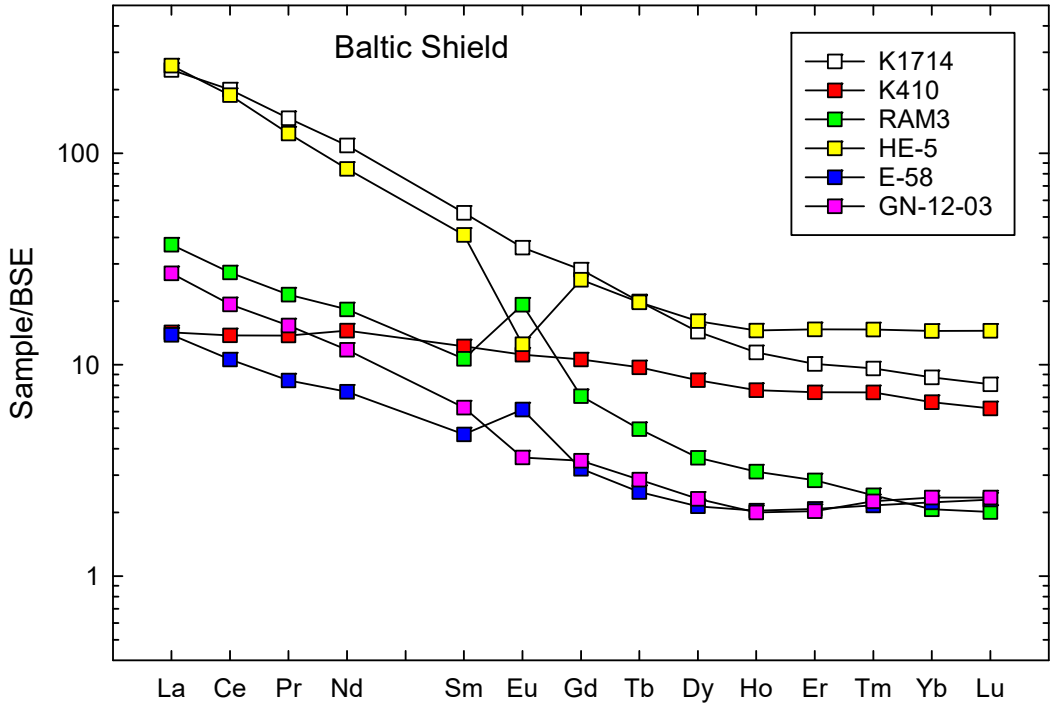

Fig. S15. Plot of REEs for samples from the Baltic Shield. The ages of the samples range from 300 Ma to 1.9 Ga.

8. Measurements of standards

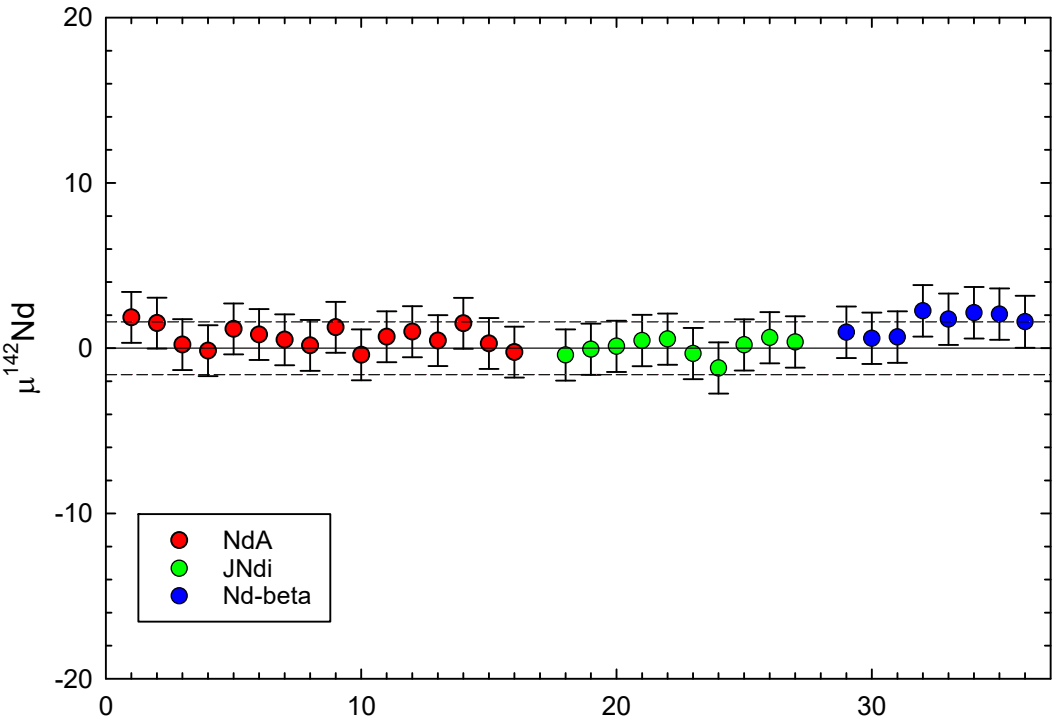

Fig. S16. Measurements of various standards and their 2σ external errors. The measurements of all the standards agree well within one another to within an external reproducibility level of a 2σ standard deviation of ±1.7 ppm. The average for each of the standards are 1.1418403 for Nd-A ($2\sigma_m$ = 0.34 ppm), 1.1418395 for JNdi-1 ($2\sigma_m$ = 0.35), and 1.1418412 for Nd-β ($2\sigma_m$ = 0.48) when the data is reduced through Reduction Method 2 (RED2) (see **Table S6**).

9. Comparison of our MORB and OIB data with those from other studies

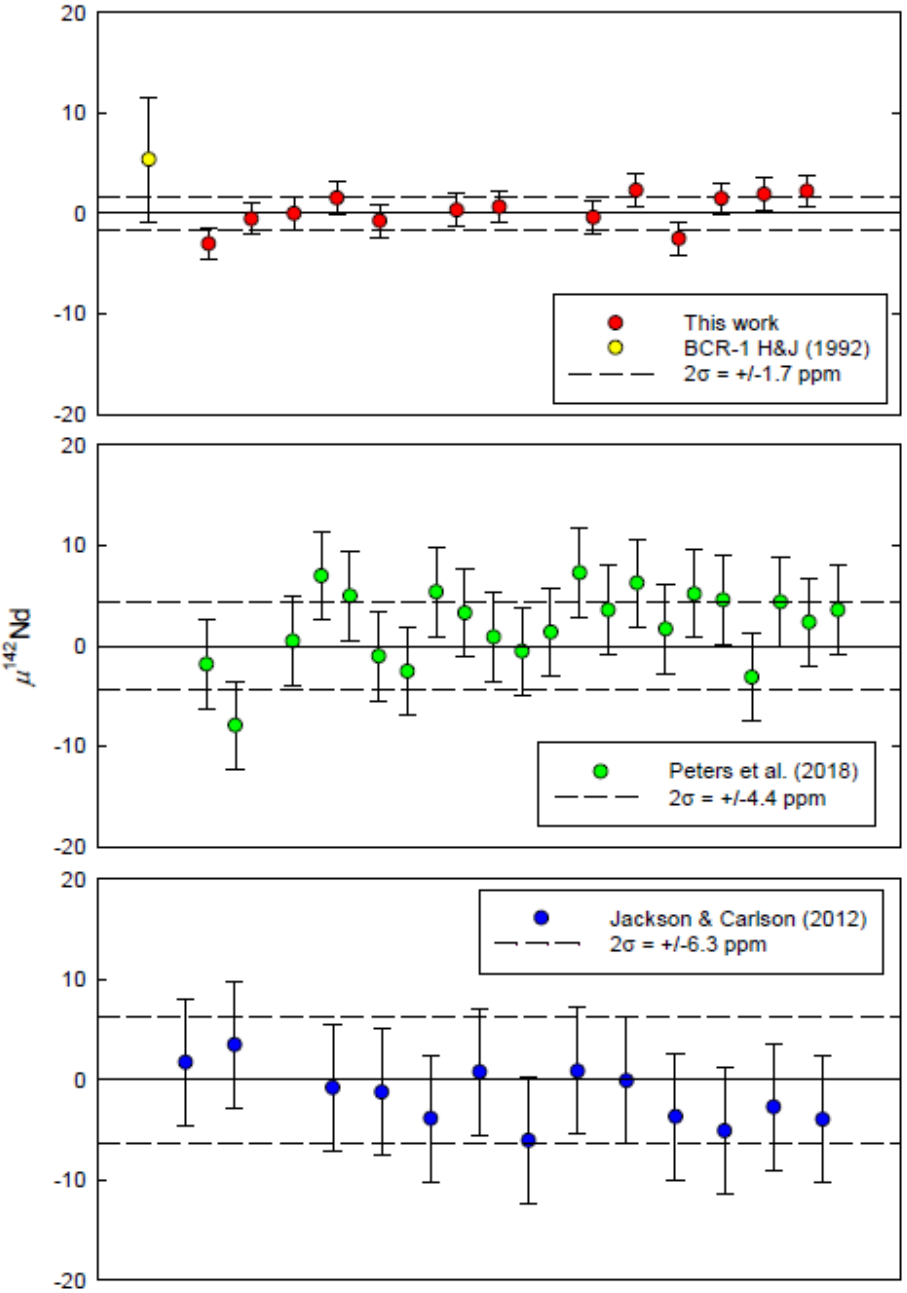

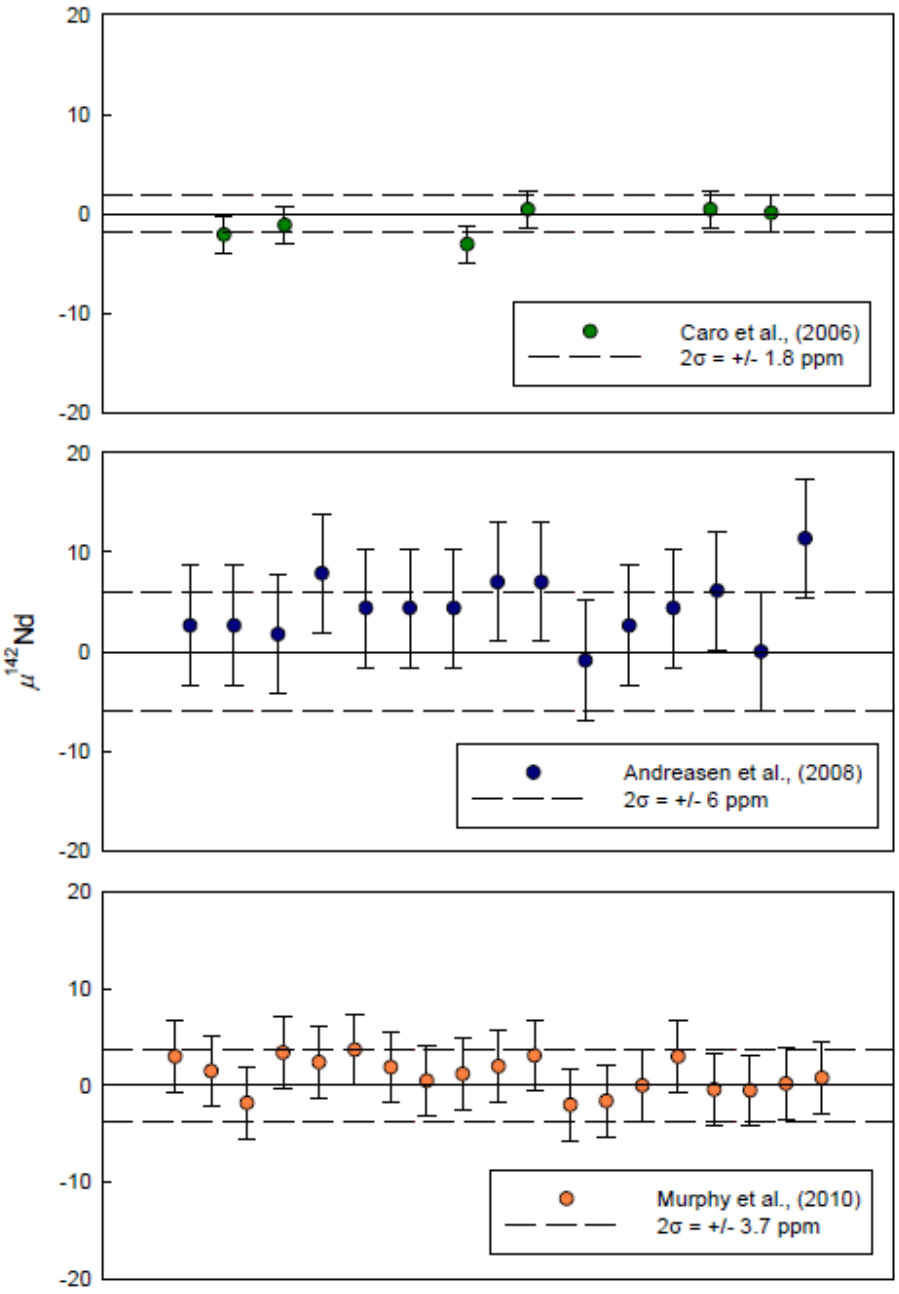

Fig. S17. Comparison of our $^{142}Nd/^{144}Nd$ data with published studies of modern-day samples from multiple labs (14, 25, 47–50). The measurement of a modern day terrestrial sample from Reference (14) is abbreviated "H&J (1992)." The error bars show external reproducibility for each of the studies (2σ). For repeat measurements of samples, the averages of multiple measurements are displayed.

10. Data tables and figures for samples and standards

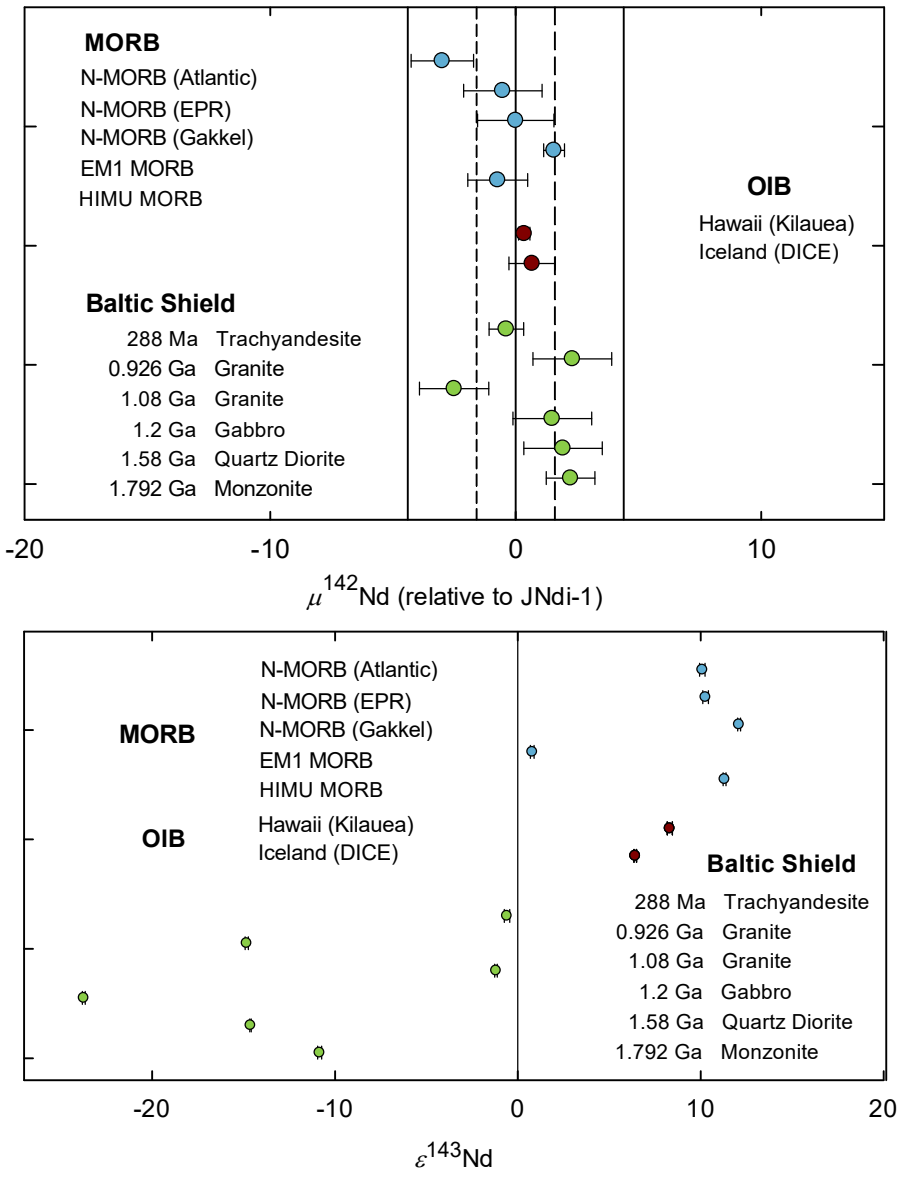

Fig. S18. Supplementary panel to **Fig. 2** in the original text, to include ε^{143}Nd values for the samples.

Table S5. Major and trace element compositions of the samples

	HLY102-096	BHVO-2	DICE	RC2D-1	CH59-2	KN 207-2	A12DR44	K1714	K410	RAM-3	HE-5	E-58	GN-12-03
Major oxides (wt%)													
SiO_2	50.36	49.46	52.27	48.69	49.33	50.82	45.71	52.31	44.66	58.19	68.13	67.96	69.32
TiO_2	1.84	2.77	0.58	1.07	2.08	1.47	2.45	1.61	2.15	0.95	0.53	0.36	0.22
Al_2O_3	16.44	14.42	9.84	18.59	14.66	15.53	17.72	19.86	16.28	19.68	15.21	13.98	16.56
FeO	9.28	10.97	9.10	7.81	11.82	9.46	6.91	5.62	13.77	3.98	3.13	6.98	1.96
MnO	0.16	0.17	0.17	0.15	0.21	0.17	0.13	0.14	0.20	0.09	0.06	0.15	0.04
MgO	7.45	7.41	16.31	8.36	7.28	8.47	9.03	1.53	9.32	1.09	0.69	1.79	0.57
CaO	10.04	11.45	10.48	12.55	11.32	10.74	11.89	6.30	9.74	2.59	2.12	4.73	2.56
Na_2O	3.68	2.45	1.24	2.61	2.95	3.04	3.22	6.30	2.87	5.48	3.65	3.39	4.71
K_2O	0.45	0.63	0.02	0.07	0.14	0.14	2.24	5.54	0.65	7.71	6.33	0.47	3.99
P_2O_5	0.30	0.28	0.02	0.10	0.20	0.16	0.70	0.79	0.35	0.24	0.14	0.19	0.08
Elements (ppm)													
Li	6.92	4.18	2.00	4.68	7.29	6.36	5.04	24.7	5.89	9.23	30.1	6.16	26.6
Be	0.77	0.82	0.07	0.81	0.63	0.45	1.92	9.58	0.86	0.99	5.69	1.34	1.53
B	8.18	0.32	3.48	4.77	1.56	3.37	7.34	7.45	2.58	1.20	3.50	1.28	4.54
Na	27308	18166	9192	19329	21900	22534	23923	46708	21323	40644	27088	25144	34911
Mg	44941	44702	98355	50407	43873	51060	54453	9231	56203	6581	4182	10786	3412
Al	87000	76292	52081	98378	77578	82212	93797	105094	86185	104168	80504	73994	87663
P	1298	1226	84	449	879	687	3046	3453	1529	1031	625	827	354
K	3695	5222	181	615	1180	1139	18605	46018	5428	63998	52549	3902	33090
Ca	71777	81809	74926	89712	80931	76785	84962	45025	69578	18544	15152	33792	18265
Sc	33.5	31.4	30.5	31.3	43.4	38.1	32.4	11.0	28.5	11.4	6.16	16.9	3.92
Ti	11023	16586	3453	6440	12469	8812	14678	9664	12912	5678	3158	2186	1289
Mn	1274	1311	1299	1127	1659	1344	1045	1060	1556	696	497	1137	315
Fe	72112	85296	70772	60721	91915	73535	53684	43703	107040	30925	24320	54286	15249
V	266	307	205	228	377	270	224	70.7	239	34.8	26.5	44.3	9.80
Cr	262	280	597	409	227	326	300	8.27	146	29.8	56.6	36.3	39.7
Co	40.0	43.8	76.4	38.9	43.8	41.5	36.6	22.4	69.5	3.40	4.45	12.1	2.27
Ni	130	116	538	141	75	136	187	9.52	218		1.86	3.20	3.21
Cu	58.7	133	85.1	74.8	64.5	67.4	64.5	25.7	74.8	6.74	6.91	35.6	3.97
Zn	137	106	83.8	86.4	131	104	115	198	154	91.5	99.7	79.9	61.4
Ga	17.5	20.5	1.25	14.2	18.2	15.4	20.3	42.9	20.0	20.2	34.0	12.8	17.5
Rb	4.82	9.09	0.23	0.37	0.85	1.21	42.9	167	13.1	72.2	288	4.24	113
Sr	168	362	82.8	128	118	127	642	1955	235	272	195	211	338
Y	41.8	25.4	10.7	23.6	47.7	35.1	28.5	49.1	34.5	14.1	72.5	9.57	9.93

Zr	153	161	13.2	66.3	139	103	303	1372	71.7	8.13	259	4.08	54.8
Nb	9.1	17.8	0.60	1.32	2.70	2.81	68.1	203	4.30	6.22	35.5	1.61	5.04
Mo	1.13	0.90	0.54	0.67	0.57	0.46	2.23	4.53	0.66	0.79	17.4	1.01	0.77
Ag	0.060	0.079	0.003	0.019	0.055	0.046	0.107	0.271	0.053	0.039	0.090	0.001	0.027
Cd	0.161	0.087	0.067	0.115	0.158	0.118	0.134	0.164	0.123	0.035	0.045	0.039	0.039
Sn	1.23	2.01	0.48	0.84	1.43	0.98	3.41	6.08	1.15	1.02	3.62	0.41	2.03
Sb	0.045	0.162	0.03	0.067	0.041	0.043	0.098	0.360	0.162	0.036	0.075	0.131	0.115
Cs	0.0577	0.0937	0.0014	0.0038	0.0093	0.0144	0.64	2.08	0.65	0.19	2.20	1.20	7.04
Ba	71.7	133	5.08	4.54	8.1	12.1	369	1009	160	2411	735	143	580
La	7.84	14.0	0.69	2.05	4.27	3.66	44.2	161	9.23	24.0	168	8.98	17.5
Ce	20.1	33.7	2.12	6.67	14.1	11.1	88.5	335	23.1	45.8	316	17.7	32.3
Pr	3.03	4.64	0.39	1.16	2.39	1.86	10.1	37.2	3.50	5.46	31.5	2.14	3.90
Nd	15.5	22.1	2.41	6.70	13.6	10.53	40.9	136	18.1	22.8	105	9.31	14.7
Sm	4.79	5.37	0.95	2.41	4.81	3.70	7.43	21.2	4.96	4.34	16.7	1.90	2.55
Eu	1.59	1.77	0.41	0.89	1.59	1.28	2.20	5.52	1.72	2.96	1.93	0.94	0.56
Gd	6.05	5.49	1.37	3.16	6.22	4.79	6.58	15.3	5.77	3.86	13.7	1.75	1.91
Tb	1.06	0.84	0.27	0.58	1.14	0.89	0.95	1.97	0.96	0.49	1.96	0.25	0.28
Dy	6.70	4.54	1.77	3.76	7.47	5.73	5.14	9.67	5.70	2.45	10.8	1.44	1.56
Ho	1.40	0.84	0.38	0.79	1.59	1.22	0.96	1.71	1.13	0.47	2.16	0.30	0.30
Er	4.04	2.22	1.13	2.30	4.65	3.50	2.65	4.42	3.24	1.24	6.44	0.91	0.89
Tm	0.62	0.31	0.17	0.35	0.71	0.54	0.39	0.65	0.50	0.16	1.00	0.15	0.15
Yb	3.85	1.74	1.09	2.19	4.48	3.35	2.29	3.84	2.93	0.91	6.38	0.98	1.04
Lu	0.57	0.25	0.16	0.32	0.66	0.49	0.34	0.55	0.42	0.14	0.98	0.16	0.16
Hf	3.64	3.84	0.50	1.72	3.57	2.72	7.22	26.7	1.89	0.24	7.58	0.13	1.55
Ta	0.55	1.02	0.055	0.12	0.19	0.17	3.80	10.5	0.27	0.23	2.18	0.04	0.39
W	0.29	0.26	0.048	0.11	0.08	3.47	2.20		0.19	0.10	0.35	0.054	0.35
Tl	0.12	0.039	0.0013	0.013	0.011	0.011	0.090	0.059	0.11	0.43	1.98	0.033	0.93
Pb	0.87	1.98	0.096	0.28	0.52	0.46	3.11	13.7	2.40	16.0	35.3	2.74	15.3
Bi	0.014	0.011	0.0062	0.0066	0.0086	0.0070	0.0109	0.0064	0.0269	0.0039	0.0340	0.0188	0.0645
Th	0.67	1.10	0.033	0.067	0.15	0.20	4.23	28.9	0.86	0.48	95.6	0.26	3.17
U	0.29	0.36	0.010	0.055	0.067	0.067	1.05	7.37	0.29	0.17	15.2	0.12	1.10

Table S6. $^{142}Nd/^{144}Nd$ measurements of standards.

Standard	$^{142}Nd/^{144}Nd$	$^{142}Ce/^{142}Nd$	$^{144}Sm/^{144}Nd$
NdA	1.1418412	4.37E-07	7.54E-07
NdA	1.1418412	4.27E-07	6.58E-07
NdA	1.1418397	5.43E-07	6.15E-07
NdA	1.1418393	4.32E-07	5.77E-07
NdA	1.1418408	6.18E-07	4.14E-07
NdA	1.1418404	6.48E-07	1.08E-08
NdA	1.1418401	3.92E-07	2.15E-07
NdA	1.1418397	3.52E-07	5.50E-07
NdA	1.1418409	2.85E-07	3.94E-07
NdA	1.1418390	4.11E-07	4.10E-07
NdA	1.1418403	3.42E-07	3.04E-07
NdA	1.1418409	2.85E-07	3.94E-07
NdA	1.1418400	3.61E-07	6.70E-07
NdA	1.1418416	6.61E-07	6.50E-07
NdA	1.1418398	5.56E-07	5.87E-07
NdA	1.1418392	8.38E-07	7.59E-07
Mean value	**1.1418403**		
2σ (ppm)	**1.38**		
$2\sigma_m$ (ppm)	**0.34**		
$\mu^{142}Nd$	**0.66**		
JNdi-1	1.1418390	4.81E-07	6.13E-07
JNdi-1	1.1418394	5.23E-07	1.00E-06
JNdi-1	1.1418396	3.53E-07	6.35E-07
JNdi-1	1.1418400	1.42E-06	9.22E-07
JNdi-1	1.1418401	3.32E-07	7.51E-07
JNdi-1	1.1418391	6.41E-07	6.68E-07
JNdi-1	1.1418381	6.09E-07	7.16E-07
JNdi-1	1.1418397	2.67E-07	3.49E-07
JNdi-1	1.1418402	5.42E-07	9.13E-07
JNdi-1	1.1418399	4.62E-07	7.57E-07
Mean value	**1.1418395**		

2σ (ppm)	**1.12**		
$2\sigma_m$ (ppm)	**0.40**		
μ^{142}Nd	**0**		
Nd-*β*	1.1418421	4.51E-07	1.72E-07
Nd-*β*	1.1418418	7.12E-07	4.03E-07
Nd-*β*	1.1418415	5.43E-07	3.43E-07
Nd-*β*	1.1418419	4.72E-07	2.58E-07
Nd-*β*	1.1418402	3.81E-07	9.27E-08
Nd-*β*	1.1418402	4.39E-07	2.13E-07
Nd-*β*	1.1418406	8.38E-07	2.59E-07
Nd-*β*	1.1418413	5.75E-07	3.08E-07
Mean value	**1.1418412**		
2σ (ppm)	**1.34**		
$2\sigma_m$ (ppm)	**0.48**		
μ^{142}Nd	**1.49**		
	Grand Mean Standards	Grand Mean Samples (Table S6)	Grand Mean Samples & Standards
Mean value	**1.1418403**	**1.1418399**	**1.1418403**
2σ (ppm)	**1.66**	**3.43**	**2.27**
$2\sigma_m$ (ppm)	**0.29**	**0.95**	**0.33**
μ^{142}Nd	**0.66**	**0.35**	**0.58**

$^{142}Ce/^{142}Nd$ and $^{144}Sm/^{144}Nd$ in the table are the measured interference corrections that were applied to correct the raw ^{142}Nd and ^{144}Nd intensities. The $^{142}Nd/^{144}Nd$ ratios in this table were corrected for mass spectrometric mass dependent fractionation using the exponential law and $^{146}Nd/^{144}Nd = 0.7219$ using the RED2 method.
NdA is our in house Nd isotope laboratory standard.
JNdi-1 is the Nd isotope standard of the Geological Survey of Japan (51).
Nd-β is the CalTech Nd isotope standard (52).
Measurements of samples and standards were made over the course of two years, from 2015 to 2017.

Table S7. Sm-Nd isotopic measurements of oceanic basalt (0 age) and continental crust samples.

Sample name	Age (Ga)	$^{147}Sm/^{144}Nd$	$^{143}Nd/^{144}Nd$	2σ	$\varepsilon^{143}Nd(0)$	2σ	$^{142}Nd/^{144}Nd$	2σ	$\mu^{142}Nd$	2σ	N
KN207-2	0	0.2213	0.5131555	3.85E-06	10.09	0.15	1.14183605	1.18E-06	-3.02	1.03	2
CH59-2	0	0.2223	0.5131645	3.83E-06	10.27	0.15	1.14183915	2.21E-06	-0.31	1.94	1
HLY102-096	0	0.1948	0.5132583	2.14E-06	12.10	0.08	1.14183955	2.07E-06	0.04	1.81	2
A12DR44	0	0.1147	0.5126785	2.68E-06	0.79	0.10	1.14184125	1.53E-06	1.53	1.34	2
RC2D-1	0	0.2267	0.5132176	1.94E-06	11.31	0.08	1.14183935	2.21E-06	-0.13	1.94	2
DICE	0	0.2432	0.5130640	3.52E-06	8.31	0.14	1.14184023	2.17E-06	0.64	1.90	2
BHVO-2	0	0.1564	0.5129673	1.84E-06	6.42	0.07	1.14183987	2.85E-06	0.32	2.50	3
K1714	0.290	0.1027	0.5126077	3.81E-06	-0.59	0.15	1.14183903	2.00E-06	-0.41	1.75	3
HE-5	0.926	0.0971	0.5118780	2.24E-06	-14.83	0.09	1.14184210	1.20E-06	2.28	1.05	1
K410	1.200	0.1707	0.5125769	1.90E-06	-1.19	0.07	1.14184130	1.87E-06	1.58	1.64	1
GN-12-03	1.080	0.1091	0.5118885	1.09E-06	-14.62	0.04	1.14183660	1.82E-06	-2.54	1.59	2
E-58	1.580	0.1289	0.5120823	2.89E-06	-10.84	0.11	1.14184200	2.88E-06	2.19	2.52	1
RAM-3	1.792	0.1172	0.5114208	2.02E-06	-23.74	0.08	1.14184223	1.69E-06	2.49	1.48	2

Here $\varepsilon^{143}Nd(0)$ is calculated relative to $^{143}Nd/^{144}Nd = 0.512638$ for the present chondritic value and $\mu^{142}Nd(0)$ is calculated relative to $^{142}Nd/^{144}Nd = 1.1418395$ for the JNdi-1. The 2σ errors are determined by the standard deviations of multiple measurements.

Table S8. Nd model ages of crustal samples, based on sample ε^{143}Nd and Sm/Nd ratios, calculated with $^{143}Nd/^{144}Nd_{CHUR}$ = 0.512638 and $^{147}Sm/^{144}Nd_{CHUR}$ = 0.1967 (5) for the CHUR (Chondritic Uniform Reservoir) model, and $^{143}Nd/^{144}Nd_{DM}$ = 0.513151 (ε^{143}Nd = 10) and $^{147}Sm/^{144}Nd_{DM}$= 0.2136 assuming differentiation from the depleted mantle.

Samples	Age (Ga)	$^{147}Sm/^{144}Nd$	$^{143}Nd/^{144}Nd$	2σ	$\varepsilon^{143}Nd(0)$	*T*-model ages in Ga (CHUR)	*T*-model ages in Ga (DM)
E-58	1.580	0.1289	0.5120823	2.89E-06	-10.84	1.248	1.916
K410	1.200	0.1707	0.5125769	1.90E-06	-1.19	0.359	2.031
GN-12-03	1.080	0.1091	0.5118885	1.09E-06	-14.62	1.303	1.836
HE-5	0.926	0.0971	0.5118780	2.24E-06	-14.83	1.16	1.661
RAM-3	1.792	0.1172	0.5114208	2.02E-06	-23.74	2.323	2.719

The first four samples in the table above are from the Sveconorwegian sector of the Baltic Shield (53). The oldest rocks in this sector are about 1.5 to 1.6 Ga old (E-58) and represent the main stage of crustal growth in this area. There are numerous younger gabbros (K410) and granites (GN-12-03 and HE-5) intruding this older complex of high-grade metamorphic rocks. The fifth sample in this table (RAM-3) is from the Transcandinavian igneous belt at the western margin of the Svecofennian sector of the Baltic Shield. The time of extraction of the Nd in these samples from the mantle is expected to be in the middle of the range between T_{CHUR} and the T_{DM} model ages in the table above. This corresponds sufficiently well to crystallization ages in the table above for the purpose of this study.

SI References

1. Rosas JC, Korenaga J (2018) Rapid crustal growth and efficient crustal recycling in the early Earth: Implications for Hadean and Archean geodynamics. *Earth Planet Sci Lett* 494:42–49.
2. Jacobsen SB (1988) Isotopic and chemical constraints on mantle-crust evolution. *Geochemica Cosmochem Acta* 52:1341–1350.
3. Jacobsen SB, Harper CLJ (1996) Geophysical Monograph. *Earth Processes: Reading the Isotopic Code*, eds Basu A, Hart S (American Geophysical Union), pp 47–74.
4. Jacobsen SB, Wasserburg GJ (1980) A two-reservoir recycling model for mantle-crust evolution. *Proc Natl Acad Sci* 77(11):6298–6302.
5. Jacobsen SB, Wasserburg GJ (1980) Sm-Nd isotopic evolution of chondrites. *Earth Planet Sci Lett* 50(1):139–155.
6. Marks NE, Borg LE, Hutcheon ID, Jacobsen B, Clayton RN (2014) Samarium-neodymium chronology and rubidium-strontium systematics of an Allende calcium-aluminum-rich inclusion with implications for ^{146}Sm half-life. *Earth Planet Sci Lett* 405:15–24.
7. McDonough W, Sun S -s. (1995) The composition of the Earth. *Chem Geol* 120(3–4):223–253.
8. Jacobsen SB, Yu G (2015) Extinct isotope heterogeneities in the mantles of Earth and Mars: implications for mantle stirring rates. *Meteorit Planet Sci* 50(4):555–567.
9. Debaille V, et al. (2013) Stagnant-lid tectonics in early Earth revealed by ^{142}Nd variations

in late Archean rocks. *Earth Planet Sci Lett* 373:83–92.
10. O'Neil J, Carlson RW (2017) Building Archean cratons from Hadean mafic crust. *Science (80-)* 355(6330):1199–1202.
11. Reimink JR, et al. (2018) Petrogenesis and tectonics of the Acasta Gneiss Complex derived from integrated petrology and ^{142}Nd and ^{182}W extinct nuclide-geochemistry. *Earth Planet Sci Lett* 494:12–22.
12. O'Neil J, Carlson RW, Paquette JL, Francis D (2012) Formation age and metamorphic history of the Nuvvuagittuq Greenstone Belt. *Precambrian Res* 220–221:23–44.
13. Jacobsen SB, Dymek RF (1988) Nd and Sr isotope systematics of clastic metasediments from Isua, West Greenland: Identification of pre-3.8 Ga Differentiated Crustal Components. *J Geophys Res Solid Earth*:338–354.
14. Harper CLJ, Jacobsen SB (1992) Evidence from coupled ^{147}Sm-^{143}Nd and ^{146}Sm-^{142}Nd systematics for very early (4.5-Gyr) differentiation of the Earth's mantle. *Nature* 360:726–732.
15. Jacobsen SB (1988) Isotopic constraints on crustal growth and recycling. *Earth Planet Sci Lett* 90:315–329.
16. Jacobsen SB, Harper CL (1996) Earth Processes: Reading the Isotopic Code. eds Basu A, Hart S (Geophysical Mongraph 95).
17. Blichert-Toft J, Albarede F (2008) Hafnium isotopes in Jack Hills zircons and the formation of the Hadean crust. *Earth Planet Sci Lett* 265:686–702.
18. Harrison TM (2009) The Hadean Crust: Evidence from >4 Ga Zircons. *Annu Rev Earth Planet Sci* 37:479–505.
19. Hyung E, Huang S, Petaev MI, Jacobsen SB (2016) Is the mantle chemically stratified? Insights from sound velocity modeling and isotope evolution of an early magma ocean. *Earth Planet Sci Lett* 440:158–168.
20. Vervoort JD, Patchett PJ (1996) Behavior of hafnium and neodymium isotopes in the crust: constraints from Precambrian crustally derived granites. *Geochemica Cosmochem Acta* 60:3717–3733.
21. Korenaga J (2018) Estimating the formation age distribution of continental crust by unmixing zircon ages. *Earth Planet Sci Lett* 482:388–395.
22. Armstrong R (1991) The persistent myth of crustal growth. *Aust J Earth Sci* 38:613–630.
23. Kellogg JB, Jacobsen SB, O'Connell RJ (2002) Modeling the distribution of isotopic ratios in geochemical reservoirs. *Earth Planet Sci Lett* 204(1–2):183–202.
24. Kellogg JB, Jacobsen SB, O'Connell RJ (2007) Modeling lead isotopic heterogeneity in mid-ocean ridge basalts. *Earth Planet Sci Lett* 262(3–4):328–342.
25. Peters BJ, Carlson RW, Day JMD, Horan MF (2018) Hadean silicate differentiation preserved by anomalous ^{142}Nd/^{144}Nd ratios in the Réunion hotspot source. *Nature* 555(7694):89–93.
26. Ashwal LD, Wiedenbeck M, Torsvik TH (2017) Archaean zircons in Miocene oceanic hotspot rocks. *Nat Commun* 8:1–9.
27. Gale A, Dalton CA, Langmuir CH, Su Y, Schilling J (2013) The mean composition of ocean ridge basalts. doi:10.1002/ggge.
28. Albarede F, et al. (1997) The Geochemical Regimes of Piton de la Fournaise Volcano (Reunion) During the Last 530,000 Years. *J Petrol* 38(2):171–201.
29. Rudnick RL, Gao S (2003) *Composition of the Continental Crust . Treatise Geochem 3 : 1-64 Composition of the Continental Crust* (Elsevier Ltd.). 2nd Ed. doi:10.1016/B978-0-

08-095975-7.00301-6.
30. Fisk MR, Upton BGJ, Ford CE (1988) Geochemical and Experimental Study of the Genesis of Magmas of Reunion Island, Indian Ocean. *J Geophys Res* 93:4933–4950.
31. Fretzdorff S, Haase KM (2002) Geochemistry and petrology of lavas from the submarine flanks of Reunion Island (western Indian Ocean): implications for magma genesis and the mantle source. *Mineral Petrol* 75:153–184.
32. Russell W, Papanastassiou D, Tombrello T (1978) Ca isotope fractionation on the Earth and other solar system materials. *Geochim Cosmochim Acta* 42(8):1075–1090.
33. Garçon M, et al. (2018) Factors in fluencing the precision and accuracy of Nd isotope measurements by thermal ionization mass spectrometry. *Chem Geol* 476(November 2017):493–514.
34. Sohn RA, et al. (2008) Explosive volcanism on the ultraslow-spreading Gakkel ridge, Arctic Ocean. *Nature* 453:1236–1238.
35. Schilling JG, et al. (1995) Thermal Structure of the Mantle beneath the Equatorial Mid-Atlantic Ridge - Inferences from the Spatial Variation of Dredged Basalt Glass Compositions. *J Geophys Res Earth* 100(B6):10057–10076.
36. Schilling J, Hanan BB, Mccully B, Kingsley RH (1994) Influence of the Sierra Leone mantle plume on the equatorial Mid-Atlantic Ridge: A Nd-Sr-Pb isotopic study. *J Geophys Res* 99(94):5–12.
37. Harrison D, Burnard P, Turner G (1999) Noble gas behaviour and composition in the mantle: Constraints from the Iceland plume. *Earth Planet Sci Lett* 171(2):199–207.
38. Ballentine CJ, Barfod DN (2000) The origin of air-like noble gases in MORB and OIB. *Earth Planet Sci Lett* 180:39–48.
39. Mukhopadhyay S (2012) Early differentiation and volatile accretion recorded in deep-mantle neon and xenon. *Nature* 486(7401):101–104.
40. Weiss D, Kieffer B, Maerschalk C, Pretorius W, Barling J (2005) High-precision Pb-Sr-Nd-Hf isotopic characterization of USGS BHVO-1 and BHVO-2 reference materials. *Geochem Geophys Geosyst* 6.
41. Andersen T, Sundvoll B (1995) Neodymium isotope systematics of the mantle beneath the Baltic shield: Evidence for depleted mantle evolution since the Archean. *Lithos* 35:235–243.
42. Jacobsen SB, Heier KS (1978) Rb-Sr isotope systematics in metamorphic rocks, Kongsberg sector, south Norway. *Lithos* 11:257–276.
43. Corfu F (2004) U–Pb Age, Setting and Tectonic Significance of the Anorthosite-Mangerite-Charnockite-Granite Suite, Lofoten-Vesteralen, Norway. *J Petrol* 45:1799–1819.
44. Jaret SJ, Hemming SR, Rasbury ET, Ramezani J, Jacobsen SB (2016) The Case for an Impact at the Gardnos Impact Structure at 385 Ma. *79th Annual Meeting of the Meteoritical Society*, p LPI Contribution No. 1921, id.6476.
45. Andersen T (1997) Radiogenic isotope systematics of the Herefoss granite, South Norway: an indicator of Sveconorwegian (Grenvillian) crustal evolution in the Baltic Shield. *Chem Geol* 135:139–158.
46. Sundvoll B, Neumann E-R, Larsen BT, Tuen E (1990) Age relations among Oslo Rift magmatic rocks: implications for tectonic and magmatic modelling. *Tectonophysics* (178):67–87.
47. Jackson MG, Carlson RW (2012) Homogeneous superchondritic $^{142}Nd/^{144}Nd$ in the mid-

ocean ridge basalt and ocean island basalt mantle. *Geochemistry, Geophys Geosystems* 13(6):1–10.
48. Murphy DT, Brandon AD, Debaille V, Burgess R, Ballentine C (2010) In search of a hidden long-term isolated sub-chondritic $^{142}Nd/^{144}Nd$ reservoir in the deep mantle: Implications for the Nd isotope systematics of the Earth. *Geochim Cosmochim Acta* 74(2):738–750.
49. Andreasen R, Sharma M, Subbarao KV, Viladkar SG (2008) Where on Earth is the enriched Hadean reservoir? *Earth Planet Sci Lett* 266(1–2):14–28.
50. Caro G, Bourdon B, Birck J-L, Moorbath S (2006) High-precision $^{142}Nd/^{144}Nd$ measurements in terrestrial rocks: Constraints on the early differentiation of the Earth's mantle. *Geochim Cosmochim Acta* 70(1):164–191.
51. Tanaka T, et al. (2000) JNdi-1: a neodymium isotopic reference in consistency with LaJolla neodymium. *Chem Geol* 168:279–281.
52. Wasserburg GJ, Jacobsen SB, DePaolo DJ, McCulloch MT, Wen T (1981) Precise determination of Sm/Nd ratios, Sm and Nd isotopic abundances in standard solutions.. Geochimica et Cosmochimica Acta. *Geochemica Cosmochem Acta* 45:45: 2311-2323.
53. Bingen B, Viola G (2018) The early-Sveconorwegian orogeny in southern Norway: Tectonic model involving delamination of the sub-continental lithospheric mantle. *Precambrian Res* 313(May):170–204.